The Thesis Committee for Tobias Köhne certifies that this is the approved version of the following thesis:

A Simulation Study Towards Local Mass Anomaly Estimation Using GRACE Data

Approved by the

Supervising Committee:

Srinivas V. Bettadpur, Supervisor

Himanshu V. Save

A Simulation Study Towards Local Mass Anomaly Estimation Using GRACE Data

by

Tobias Köhne

Thesis

Presented to the Faculty of the Graduate School
of the University of Texas at Austin
in Partial Fulfillment
of the Requirements
for the Degree of

Master of Science in Engineering

The University of Texas at Austin
December 2018

Acknowledgments

I would like to begin by sincerely thanking my advisor Dr. Srinivas Bettadpur for leading me into the world of Orbital Mechanics and Earth Sciences. He trusted in my ability to pursue a career in academia, and enabled my dream to get a master's degree in the United States. It has been an honor to work with such a leading figure in gravity field research, and I will be forever grateful.

I would also like to acknowledge Dr. Himanshu Save for offering his vast expertise and providing invaluable suggestions as my second reader. Additionally, I would like to thank the entirety of the incredibly welcoming and supportive people at the Center for Space Research, and all of the amazing faculty of the Aerospace Engineering department I had the fortune to learn from.

On a personal note, I want to thank my friends in Austin for their encouragement, their help, and ultimately making Texas become home. Lastly, I want to thank my family, who always made me forget the big pond between us. Their support is amazing – Ihr seid die Besten!

Tobias Köhne

A Simulation Study Towards Local Mass Anomaly Estimation Using GRACE Data

by

Tobias Köhne, M.S.E.
The University of Texas at Austin, 2018
Supervisor: Srinivas V. Bettadpur

Since the dawn of spaceborne Earth Science missions like the Gravity Recovery and Climate Experiment (GRACE), our understanding of global geophysical processes has increased significantly. As measurements get more precise, it is necessary to improve the accuracy of our models to explain observations more precisely. In the case of GRACE-produced gravity solutions, postfit residuals show spatial patterns that indicate unmodeled influences and motivate further investigation.

The purpose of this work is to assess the potential of dividing Earth into a grid and using GRACE observations to investigate local mass anomalies, in contrast to the global fields generated usually. Starting from the equations of motion of the N-body problem, a framework is developed and implemented to allow for the simulation of GRACE-like orbits, and generation of inter-satellite range measurements. After differentiating twice using a digital filter, the acceleration observables can be used to estimate excess or default mass, as they are proportional to the forces acting on the spacecraft.

Using analytical formulations to generate the true inter-satellite range accelerations, grid-by-grid least squares solutions allow for the estimation of the respective

local mass anomaly. However, as there is no knowledge about the true accelerations in reality, this only proves theoretical feasibility. When imitating the process flow of GRACE to generate observed range accelerations from range measurements, numerical insufficiencies stemming from a suboptimal orbit propagator are too large to yield accurate and stable estimates. A sensitivity analysis is included to determine the impact of several simulation parameters and inform future studies of critical design choices, if any emerge.

Lastly, an effort is made to search for unmodeled forces in GRACE acceleration residuals. Applying the same grid-based models as used in the simulation setup, a curve is fit through the data spanning the entire mission. The result is a global, coarse estimate of the location and amplitude of model inaccuracies, serving as a starting point for future studies into their causes.

Table of Contents

List of Tables

List of Figures

Chapter 1

Introduction

Earth's gravity field is a manifestation of the multitude of geophysical processes that are occurring on our planet. As mass is redistributed on local to global scales, Earth's non-uniform gravitational potential changes with it. The most prominent influences arise from oceanic and atmospheric tides, melting ice sheets, tectonic movement and the land water cycle. Knowledge about these processes is necessary for a variety of applications, ranging from coastal tide forecasts to precise global positioning, climate variability and sea level change. Improving underlying models directly affects the precision and accuracy of any derived application [1].

Evidence exists of regions around the globe where current models exhibit larger uncertainties than average, and the Eastern coast of Greenland is one of them. The case of Joseph Fjord is presented in Section 1.1 to motivate the study of regional mass anomalies. However, the size and remoteness of Greenland's fjords and its larger neighbors make it hard to observe their behavior locally. Instead, low-Earth orbiting satellites like GRACE, CryoSat-2 or ICESat can be used because of their unique possibilities of regular flyovers and a diverse array of instruments. In Section 1.2, the GRACE spacecraft specifically are introduced as one of the viable remote sensing missions to further investigate regional mass anomalies. Finally, Section 1.3 defines the goals of this preliminary study of feasibility, and Section 1.4 provides an outline of the work.

1.1 Motivation

Common mean sea surface height models have issues accurately representing sea level in coastal regions such as around Greenland's East coast [2]. An analysis using interferometric Synthetic Aperture Radar (inSAR) aboard the CryoSat-2 satellite showed that the mean sea level decreases significantly when moving from the open ocean through the 200 km long Kaiser Franz Joseph Fjord. Simultaneously, mean sea surface (MSS) and geoid models show discrepancies between each other of up to one meter. This led to the conclusion that existing models do not fully explain the processes and mean states in regions with complex coastline geometries such as fjords and sounds.

This problem also exists at larger scales, as can be seen by spatial patterns in GRACE data. After solving for a gravity field model using GRACE, taking into account existing background models and instrument calibration parameters, postfit residuals represent noise and any other influence that could not be explained by the force models. Plotting them on a global grid reveals areas that have larger-than-usual standard deviations or non-zero means, indicating that the underlying processes in that particular region are not fully understood (see Figure 1.1).

Lastly, current global gravity models have spatial resolutions much larger than typical coastline geometries, and only the world's largest fjords, like Scoresby Sound, are of comparable size. Additionally, spherical harmonics based gravity products are usually smoothed to at least 50 km. Thus, when coastal processes differ from open ocean dynamics, the resulting signals in gravity field estimates are lost.

It is therefore warranted to search for other ways to improve our current understanding of local anomalous processes for remote sensing.

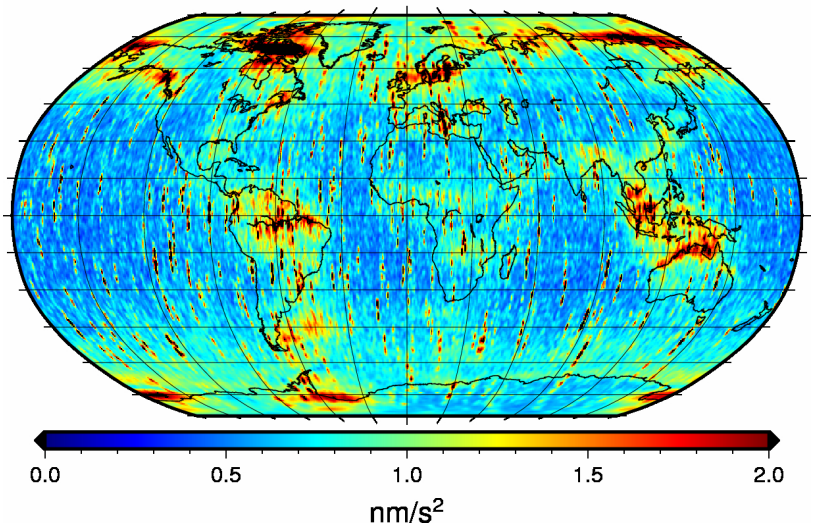

Figure 1.1: Global Range Acceleration Postfit Residuals Standard Deviation. 0.5 deg grid, 200 km smoothing, year 2008. North-South striping occurs as a data artifact.

1.2 The GRACE Mission

The Gravity Recovery and Climate Experiment (GRACE) mission was jointly launched in March 2002 by NASA and DLR under the NASA Earth System Science Pathfinder Program to study Earth's time-varying gravity field with unprecedented accuracy. The twin satellites followed each other on a near-circular, near-polar orbit at an altitude of initially 500 km, and separated by approximately 220 km, until the end of the mission in October 2017 [3]. As the satellites would pass over gravity anomalies (with respect to a uniform gravity field of a spherical, homogeneous Earth), each of them would experience different gravitational accelerations from the planet below, thus deviating from their nominal orbit and affecting the inter-satellite range. These effects were measured to micrometer precision using microwave ranging instruments on both satellites.

To isolate gravitational accelerations from non-gravitational ones like residual

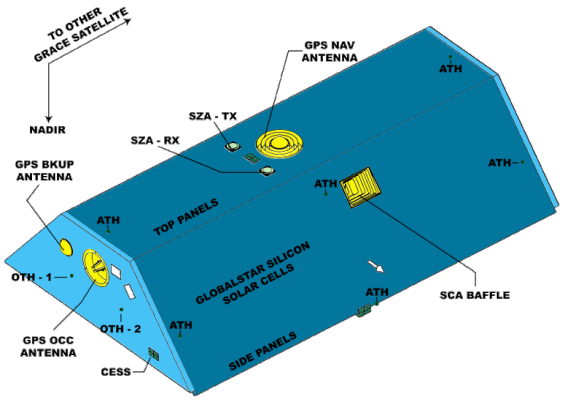

(a) Top View

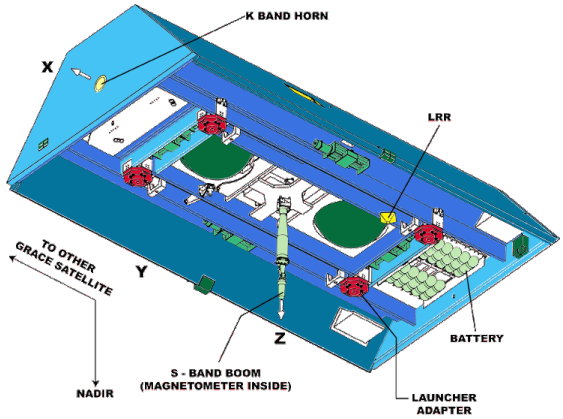

(b) Bottom View

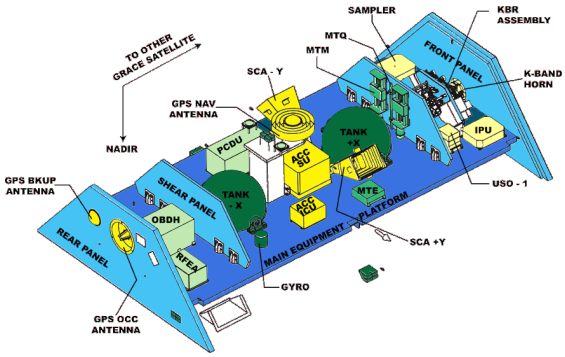

(c) Internal View

Figure 1.2: GRACE Spacecraft Components [4]

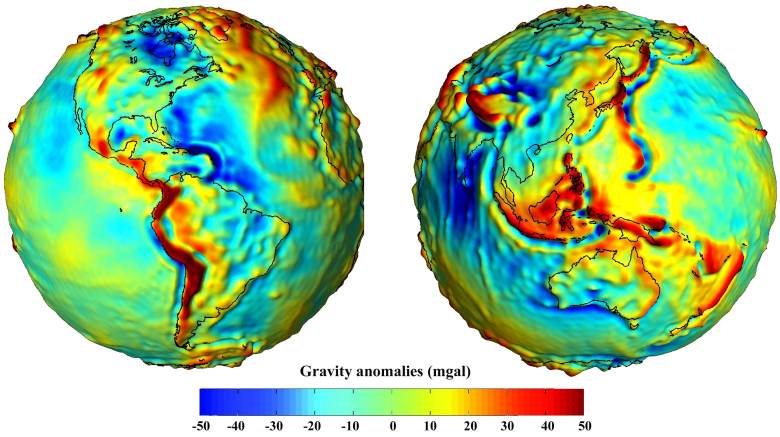

Figure 1.3: Earth's Gravity Field Anomalies [5]

atmospheric drag and solar radiation pressure, each satellite included highly sensitive onboard accelerometers (which do not experience gravity gradients). Furthermore, the spacecraft included GPS receivers to track their orbit and enable precise timing, and star trackers for attitude determination (see Figure 1.2). GRACE was the first mission to generate a global gravity field (see Figure 1.3) without using other satellite or in-situ data, and did so much more precisely than any previously released model [6].

Gravity field models like the ones produced by the Center for Space Research (CSR) at UT Austin can be computed in two distinct ways: using spherical harmonics (SH, [7]) or mass concentration blocks (mascons, [8]). SH are a computationally efficient way of analytically describing the surface of a sphere using orthogonal sinusoidal basis functions wrapping around the body. The wavelengths of the underlying functions decrease with increasing degree and order, making it possible to (theoretically) model features in size from global (the size of the sphere) to infinitely small. In practice and without combining data sources, GRACE gravity fields are estimated up to degree 180 (corresponding to a wavelength of $2\,\text{deg} \approx 222$ km).

Mascons, in contrast, discretize the surface of the body into a grid of independent masses and estimate each individual influence on the satellite. While easier to visualize and model, it is a purely numerical approach and only rendered feasible in the last years with increasing computing power. Advantages include the possibility to attribute constraints on the behavior of each mascon (e.g., grid points on land have different dynamics than open ocean grid points).

When estimating gravity field solutions with spacecraft on polar orbits, erroneous gravity anomalies appear as global North-South stripes. These need to be reduced by post-processing (e.g., Gaussian spatial smoothing), or avoided by using regularization schemes in the estimation process [9, Ch. 3.1].

1.3 Goals

The goal of this work is to study the use of GRACE observations to estimate localized mass anomalies using gridded simulations. A simplified model is used that includes Earth as a point mass, two satellites and a specified number of mass anomalies distributed on Earth's surface. Orbits are propagated numerically, and observations are generated to estimate the anomaly's mass variations in a least squares problem setup. To imitate a grid-wise estimation distributed over Earth's surface, the observations are regionally restricted to an area close to the mascon. Furthermore, the input data rate is increased from currently 0.2 Hz to the native measurement rate of 10 Hz in order to avoid observability issues inside each grid element. Lastly, the influence of several parameters in the simulation setup is assessed to inform possible future studies using GRACE data.

If successful, the estimation of anomalous mass variations on an independent, per-grid-element basis could enable the investigation into local signals that would

otherwise get lost in the global monthly gravity field estimates. By extending the time span available to each grid's solution, using observations spanning years instead of a month, enough data is available to (theoretically) avoid any aliasing problems. Then, the integration of local mass variation patterns into existing background models could improve any application relying on them.

1.4 Outline

The mathematical foundation for this work is laid in Chapter 2. First, the equations of motion for a body under the gravitational influence of multiple point masses (the N-Body problem) are derived. In the case of the GRACE satellites, densely distributed mass anomalies on Earth's surface can be considered equivalent to the complex gravitational potential they experience. The equations are then re-arranged to allow for a least squares formulation, enabling the estimation of the variability in the mascons affecting the spacecraft. The chapter concludes by giving a detailed description of the coding practice used to simulate and solve such a scenario, as well as how it needs to be adapted to make use of GRACE observations.

Further details about the ranging instrument onboard and subsequent ground processing is given in Chapter 3. The main focus is on the presentation of the digital filter used to generate the range acceleration observable from range measurements or nominal orbits. It is then argued that it does not perform adequately when used on data from simplified simulations such as used in this work. Therefore, analytically generated observables will be used to assess simulation performance, as it can be assumed that future, appropriate orbit propagation would remove any major issues.

Following a short introduction to tidal theory, the simulation runs for this study are shown in Chapter 4. A general baseline case is presented for reference,

and various performance characteristics are introduced to allow for a meaningful comparison between simulations. Furthermore, a selection of test cases is used to assess the influence of different simulation parameters. Finally, an attempt at isolating and estimating unmodeled accelerations is made using GRACE data.

Summarizing the results and proposing a way forward for future work, Chapter 5 wraps up this study.

Chapter 2

Mass Concentration Estimation

This chapter serves to derive the mathematical foundation for, and present the implementation of, tidal estimation using mass concentrations. In Section 2.1, the necessary equations of motion for a satellite affected by a point mass and spherically distributed, time-varying mass concentrations on its surface are developed. In Section 2.2, these are then used to formulate a least-squares problem to estimate the mass parameters given the range acceleration between two satellites. Finally, the implementation is presented in Section 2.3.

2.1 The N-Body Problem

Given an arbitrary vector $\vec{y}$, denote its norm without an arrow, and its corresponding unit vector with a hat, i.e.

$$\vec{y} = y\hat{y}$$

Consider a system of point masses m_i with inertial coordinates $\vec{r}_i$ under mutual gravitational attraction. Define the distance between two masses i and j as

$$\vec{r}_{ij} = \vec{r}_j - \vec{r}_i$$

Following Newton's Universal Law of Gravitation, the force $\vec{f}_{ij}$ acting on a particle i due to another particle j with masses m_i and m_j, and inertial position $\vec{r}_i$ and $\vec{r}_j$,

respectively, is

$$\vec{f_{ij}} = Gm_i m_j \frac{\hat{r}_{ij}}{r_{ij}^2}$$

Using Newton's Second Law of Motion, the acceleration of the particle (i.e., the second time derivative of its position) due to the force $\vec{f_{ij}}$ can be expressed as

$$\ddot{\vec{r}}_i = \vec{a}_i = \frac{\vec{f_{ij}}}{m_i} = Gm_j \frac{\hat{r}_{ij}}{r_{ij}^2}$$

where G is the gravitational constant. If multiple point masses j act on particle i simultaneously, the total force, and therefore acceleration, is the sum of each individual force:

$$\ddot{\vec{r}}_i = \frac{1}{m_i} \sum_j \vec{f_{ij}} = \sum_j Gm_j \frac{\hat{r}_{ij}}{r_{ij}^2} \tag{2.1}$$

Assume now that Earth is a sphere of constant mass density and is covered by equally-spaced, densely packed particles that account for the time-varying mass distribution in Earth's outer crust and lower atmosphere. The constant part can then be represented mathematically equivalent by a point mass at Earth's center of mass. "Densely packed" in this context means that a spacecraft in orbit would not experience a significantly different orbit if the spacing would be further decreased. Therefore, Earth's time-varying mass distribution can be approximated by a system of N_E particles, consisting of one central mass and $N_E - 1$ mass particles equally distributed on a sphere of Earth's radius. (2.1) is then the equation of motion for a satellite around Earth, and can be used to simulate the satellite's orbits. Note that this includes the assumption that the $N_E - 1$ surface mass particles do not influence Earth's behavior (deformation, mass transport or center of mass movement) in any

significant way, which is reasonable because of the orders of magnitudes in difference between them.

The instantaneous orbit of a satellite is completely defined by its position and velocity, as they constrain all six degrees of freedom. Mathematically, the second-order differential equation (2.1) is sufficient to integrate a set of initial conditions to generate an orbit, but numerically, it is easier to use a system of first-order differential equations instead. Defining the augmented state

$$\vec{y} = \begin{bmatrix} \vec{r} \\ \dot{\vec{r}} \end{bmatrix}$$

allows to reformulate the equations of motion using only first-order derivatives:

$$\dot{\vec{y}} = \begin{bmatrix} \dot{\vec{r}} \\ \ddot{\vec{r}} \end{bmatrix} = \begin{bmatrix} \dot{\vec{r}} \\ \sum_j G m_j \frac{\hat{r}_{ij}}{r_{ij}^2} \end{bmatrix} \tag{2.2}$$

which will be used for all numerical integration in this work.

2.2 Estimation Formulation

To estimate time-varying mass fields, GRACE produces scalar range measurements of the distance between the two satellites. To solve the estimation problem, a formulation needs to be developed that connects the measurements to Earth's varying mass. The equations of motion (2.1) are linear in mass, but include the three-dimensional relative acceleration of the satellites. The goal is a formulation of the form $\vec{z} = H\vec{x}$, where $\vec{z}$ are stacked, scalar observables, H is the mapping matrix of partials, and $\vec{x}$ includes the parameters to be estimated.

Consider the two GRACE satellites (labeled A and B) in orbit: they are attracted by the N_E point mass system representing Earth, in addition to being attracted to each other. Let $\vec{r}_A$ and $\vec{r}_B$ be their position in Earth Centered Inertial (ECI) coordinates, respectively.

$$\ddot{\vec{r}}_A = -\sum_{j=0}^{N_E-1} Gm_j \frac{\hat{r}_{jA}}{r_{jA}^2} - Gm_B \frac{\hat{r}_{BA}}{r_{BA}^2}$$
$$\ddot{\vec{r}}_B = -\sum_{j=0}^{N_E-1} Gm_j \frac{\hat{r}_{jB}}{r_{jB}^2} - Gm_A \frac{\hat{r}_{AB}}{r_{AB}^2}$$

Their relative (three-dimensional) acceleration can then be written as

$$\ddot{\vec{\rho}} = \ddot{\vec{r}}_{AB} = \ddot{\vec{r}}_B - \ddot{\vec{r}}_A = \sum_{j=0}^{N_E-1} Gm_j \left(\frac{\hat{r}_{jA}}{r_{jA}^2} - \frac{\hat{r}_{jB}}{r_{jB}^2} \right) - G\left(m_A + m_B\right) \frac{\hat{\rho}}{\rho^2} \tag{2.3}$$

For a standard GRACE orbit, the height of the satellites is approximately 300 to 500 km above ground, and they are separated by about 200 to 300 km. The attraction between the satellites is negligible compared to the attraction of Earth. Thus, one can assume that the relative acceleration follows

$$\ddot{\vec{\rho}} \approx \sum_{j=0}^{N_E-1} Gm_j \left(\frac{\hat{r}_{jA}}{r_{jA}^2} - \frac{\hat{r}_{jB}}{r_{jB}^2} \right) \tag{2.4}$$

In the next steps, the scalar inter-satellite range acceleration is derived (closely following [10]) and the connection to (2.4) is shown. (2.5) defines relative distance,

velocity and acceleration in an inertial frame.

$$\vec{\rho} = \rho\hat{\rho} = \vec{r}_{AB} = \vec{r}_B - \vec{r}_A \tag{2.5a}$$

$$\dot{\vec{\rho}} = \frac{d}{dt}\vec{\rho} = \frac{d}{dt}\left(\vec{r}_B - \vec{r}_A\right) = \dot{\vec{r}}_B - \dot{\vec{r}}_A \tag{2.5b}$$

$$\ddot{\vec{\rho}} = \frac{d^2}{dt^2}\vec{\rho} = \frac{d^2}{dt^2}\left(\vec{r}_B - \vec{r}_A\right) = \ddot{\vec{r}}_B - \ddot{\vec{r}}_A \tag{2.5c}$$

Using these definitions, the scalar range and range rate can be formulated (2.6)-(2.7):

$$\rho = \vec{\rho} \cdot \hat{\rho} \tag{2.6}$$

$$\dot{\rho} = \frac{d}{dt}\rho = \frac{d}{dt}\left(\vec{\rho} \cdot \hat{\rho}\right) = \dot{\vec{\rho}} \cdot \hat{\rho} + \vec{\rho} \cdot \dot{\hat{\rho}} \tag{2.7}$$

The unit vector's time derivative $\dot{\hat{\rho}}$ needs further clarification:

$$\dot{\hat{\rho}} = \frac{d}{dt}\hat{\rho} = \frac{d}{dt}\frac{\vec{\rho}}{\rho} = \frac{\dot{\vec{\rho}}}{\rho} - \dot{\rho}\frac{\hat{\rho}}{\rho}$$

With this, the range rate can be written more concisely (2.8):

$$\dot{\rho} = \dot{\vec{\rho}} \cdot \hat{\rho} + \vec{\rho} \cdot \left(\frac{\dot{\vec{\rho}}}{\rho} - \dot{\rho}\frac{\hat{\rho}}{\rho}\right) = 2\hat{\rho} \cdot \dot{\vec{\rho}} - \dot{\rho} = \hat{\rho} \cdot \dot{\vec{\rho}} \tag{2.8}$$

The range acceleration is now:

$$\ddot{\rho} = \frac{d}{dt}\hat{\rho} \cdot \dot{\vec{\rho}} = \dot{\hat{\rho}} \cdot \dot{\vec{\rho}} + \hat{\rho} \cdot \ddot{\vec{\rho}} = \hat{\rho} \cdot \ddot{\vec{\rho}} + \frac{1}{\rho}\left(\|\dot{\vec{\rho}}\|^2 - \dot{\rho}^2\right) \tag{2.9}$$

To summarize:

$$\rho = \hat{\rho} \cdot \vec{\rho} \tag{2.10a}$$

$$\dot{\rho} = \hat{\rho} \cdot \dot{\vec{\rho}} \tag{2.10b}$$

$$\ddot{\rho} = \hat{\rho} \cdot \ddot{\vec{\rho}} + \frac{1}{\rho}\left(\|\dot{\vec{\rho}}\|^2 - \dot{\rho}^2\right) \tag{2.10c}$$

The left term in (2.10c) is the projection of the relative acceleration (2.4) onto the line of sight, whereas the second term represents the centrifugal acceleration due to the rotation of the baseline. The observable to obtain should be a linear function of only the masses. Given that the position and velocity are usually already known, the terms can be rearranged, and an intermediate observable $\Delta\ddot{\vec{\rho}}$ can be defined:

$$\Delta\ddot{\vec{\rho}} = \ddot{\rho} - \frac{1}{\rho}\left(\|\dot{\vec{\rho}}\|^2 - \dot{\rho}^2\right) = \hat{\rho} \cdot \ddot{\vec{\rho}} = \hat{\rho}^T \sum_{j=0}^{N_E-1} Gm_j \left(\frac{\hat{r}_{jA}}{r_{jA}^2} - \frac{\hat{r}_{jB}}{r_{jB}^2}\right)$$

Note that in practice, the ranging instrument only measures biased range. With numerical differentiation (see Section 3.2), $\ddot{\rho}$ can be approximated (and the constant bias disappears), which in turn allows the observable to be formed.

If the masses $j = 0 \ldots N_E - 1$ are the unknowns one is looking for, the observation equation can be rewritten as

$$\Delta\ddot{\vec{\rho}} = \hat{\rho}^T \begin{bmatrix} \left(\frac{\hat{r}_{0A}}{r_{0A}^2} - \frac{\hat{r}_{0B}}{r_{0B}^2}\right) & \cdots & \left(\frac{\hat{r}_{(N_E-1)A}}{r_{(N_E-1)A}^2} - \frac{\hat{r}_{(N_E-1)B}}{r_{(N_E-1)B}^2}\right) \end{bmatrix} \begin{bmatrix} Gm_0 \\ \vdots \\ Gm_{N_E-1} \end{bmatrix}$$

Assuming that the total mass of Earth (set $j = 0$) is a known constant, then its gravitational influence can be subtracted from the intermediate observable (given

knowledge of the satellites' position), and the residual range acceleration $\Delta\ddot{\rho}$ becomes the actual observable:

$$\Delta\ddot{\rho} = \ddot{\rho} - \frac{1}{\rho}\left(\|\dot{\vec{\rho}}\|^2 - \dot{\rho}^2\right) - Gm_0\hat{\rho}^T\left(\frac{\hat{r}_{0A}}{r_{0A}^2} - \frac{\hat{r}_{0B}}{r_{0B}^2}\right) \tag{2.11}$$

$$= \hat{\rho}^T\left[\left(\frac{\hat{r}_{1A}}{r_{1A}^2} - \frac{\hat{r}_{1B}}{r_{1B}^2}\right) \quad \cdots \quad \left(\frac{\hat{r}_{(N_E-1)A}}{r_{(N_E-1)A}^2} - \frac{\hat{r}_{(N_E-1)B}}{r_{(N_E-1)B}^2}\right)\right]\begin{bmatrix} Gm_1 \\ \vdots \\ Gm_{N_E-1}\end{bmatrix} \tag{2.12}$$

Strictly speaking, it should be noted that our knowledge of Earth's mass is only known in the form of its standard gravitational parameter $\mu = G\sum_j m_j$, which makes it not trivial to subtract a "mean" m_0 in (2.11). However, because mass variations on Earth's crust represent only a negligible fraction of Earth's total mass, this simplification is acceptable.

If the other masses follow a time-dependent function, with known structure,

each mass (omitting the index j) can be modeled as

$$
\begin{aligned}
m &= f_{Polynomial} + f_{Periodic} \\
&= \sum_{k=1}^{N_p} \left(p_k \cdot (t - t_0)^{k-1}\right) + \sum_{l=1}^{N_c} \left(a_l \sin\theta_l + b_l \cos\theta_l\right) \\
&= \underbrace{\begin{bmatrix} 1 & (t-t_0) & \dots & (t-t_0)^{N_p} & \sin\theta_1 & \cos\theta_1 & \dots & \sin\theta_{N_c} & \cos\theta_{N_c} \end{bmatrix}}_{\vec{\alpha}} \left.\begin{bmatrix} p_0 \\ p_1 \\ \vdots \\ p_{N_p} \\ a_1 \\ b_1 \\ \vdots \\ a_{N_c} \\ b_{N_c} \end{bmatrix}\right\} \vec{\beta}
\end{aligned}
\tag{2.13}
$$

where $\vec{\alpha}$ is the time-dependent, and $\vec{\beta}$ the time-independent part. The parameter vector can then be rewritten for particles $j = 1 \dots N_E - 1$ as

$$
\begin{bmatrix} m_1 \\ \vdots \\ m_{N_E-1} \end{bmatrix} = \begin{bmatrix} \vec{\alpha}_1 & & 0 \\ & \ddots & \\ 0 & & \vec{\alpha}_{N_E-1} \end{bmatrix} \begin{bmatrix} \vec{\beta}_1 \\ \vdots \\ \vec{\beta}_{N_E-1} \end{bmatrix} \tag{2.14}
$$

The resulting equation is of the form $z = Hx$ and is thus a linear system with respect to the particle parameters, solvable with the usual linear least squares methods. The

final equation is therefore:

$$\underbrace{\Delta\ddot{\rho}}_{z} = \underbrace{G\hat{r}^T \begin{bmatrix} \left(\frac{\hat{r}_{1A}}{r_{1A}^2} - \frac{\hat{r}_{1B}}{r_{1B}^2}\right) & \dots & \left(\frac{\hat{r}_{(N_E-1)A}}{r_{(N_E-1)A}^2} - \frac{\hat{r}_{(N_E-1)B}}{r_{(N_E-1)B}^2}\right) \end{bmatrix} \begin{bmatrix} \vec{\alpha}_1 & & 0 \\ & \ddots & \\ 0 & & \vec{\alpha}_{N_E-1} \end{bmatrix}}_{H} \underbrace{\begin{bmatrix} \vec{\beta}_1 \\ \vdots \\ \vec{\beta}_{N_E-1} \end{bmatrix}}_{x} \tag{2.15}$$

Note that this is a scalar equation, because H and z are of the dimensions $1 \times (N_E - 1)N_m$ and $(N_E - 1)N_m \times 1$, respectively, where $N_m = N_p + 2N_c$ is the total number of one particle's mass parameters. It is also a time-dependent equation valid at only a particular epoch, as $\vec{r}$, $\vec{r}_{jA}$, $\vec{r}_{jB}$, and $\vec{\alpha}_j$ are time-dependent. Introducing the time index $m = 1 \dots N_t$, and stacking all data points z_m and mapping rows H_m, yields the linear system

$$\underbrace{\vec{z}}_{N_t \times 1} = \underbrace{H}_{N_t \times (N_E-1)N_m} \quad \underbrace{\vec{x}}_{(N_E-1)N_m \times 1} \tag{2.16}$$

Note also that the calculation of H necessitates the knowledge of the position of each satellite and each point mass in ECI coordinates, and the constants and frequencies for every pattern the mass points are supposed to follow, see (2.13). Table 2.1 provides a summary of the indices, their range and description.

Finally, an abstraction of the above equations for range acceleration can be formulated as

$$\ddot{\rho}_{\text{Observed}} = \ddot{\rho}_{\text{True}} + \ddot{\rho}_{\text{Noise}} = \ddot{\rho}_{\text{Modeled}} + \ddot{\rho}_{\text{Residual}} \tag{2.17}$$

Index	Range	Description
i	A, B	GRACE Satellites
j	$0 \dots N_E - 1$	Point masses representing Earth
k	$1 \dots N_p$	Number of polynomial terms
l	$1 \dots N_c$	Number of periodic constituents
m	$1 \dots N_t$	Number of data points

Table 2.1: Indices used in Problem Formulation

Because gravity-induced range acceleration is linear in the masses acting on the satellites, analyzing acceleration anomalies in (2.17) acts as a proxy to estimating mass anomalies. Therefore, it is a fair assumption that any functional structure (polynomial trend, periodic oscillations etc.) of the mass would also be the functional structure of the variability of the acceleration residuals. Adapting (2.13), a fit through a time series of $\ddot{\rho}_{\text{Residual}}$ can be computed using standard least squares techniques:

$$\underbrace{\ddot{\vec{\rho}}_{\text{Residual}}}_{\vec{z}} = \underbrace{\begin{bmatrix} \vec{\alpha}_1 \\ \dots \\ \vec{\alpha}_{N_t} \end{bmatrix}}_{H} \underbrace{\vec{\gamma}}_{\vec{x}} \tag{2.18}$$

Estimating these coefficients $\vec{\gamma}$ is the purpose of the second part of the work. If $\ddot{\rho}_{\text{Residual}}$ is only white noise, all parameters $\vec{\gamma}$ will tend towards zero. Otherwise, $\vec{\alpha}(t)\vec{\gamma}$ will be the optimal estimate of the missing signal.

2.3 Implementation

This section serves to present the structure of the implemented code and explain design choices for both parts of this study. Global initializations for the simulation part (i.e., integration settings, initial conditions of the satellites, filter parame-

ters, position and amplitudes of the mass anomalies) are made before the main code is launched, and will be touched upon in the appropriate subsections. Most of the code is written in MATLAB for reasons of simplicity, and is sufficient for proof of concept purposes.

2.3.1 Orbit Simulation and Anomaly Estimation

A simplification of the simulation and estimation processes is shown in Figure 2.1, which doubles as a guide to the following subsections. The main goal of this work is to simulate and evaluate inter-satellite range accelerations between two GRACE-like satellites to assess the feasibility of localized mass anomaly estimation. Thus, the most important data to simulate are the satellite's orbits, and consequently, the measurements. Two different orbits are distinguished: a *true* orbit, and a *nominal* orbit. The former is what instruments on the satellites experience, and the latter is the closest approximation one can have of the true orbit. Orbits, measurements, observables and partials are calculated and accumulated inside a loop, where one iteration corresponds to one day. Once the loop has exited, the least squares solution using all the generated data can be computed.

True Orbit

A satellite's dynamic state and orbit is fully described by its three-dimensional position and velocity. Thus, a set of initial conditions is sufficient to propagate the state of the satellite indefinitely to generate an orbit, provided all forces acting on the satellite are known. For all simulation purposes, Earth is assumed to be homogeneous and completely spherical (i.e., one point mass at its center is a mathematically equivalent representation). A small number of mass anomalies (usually one or two)

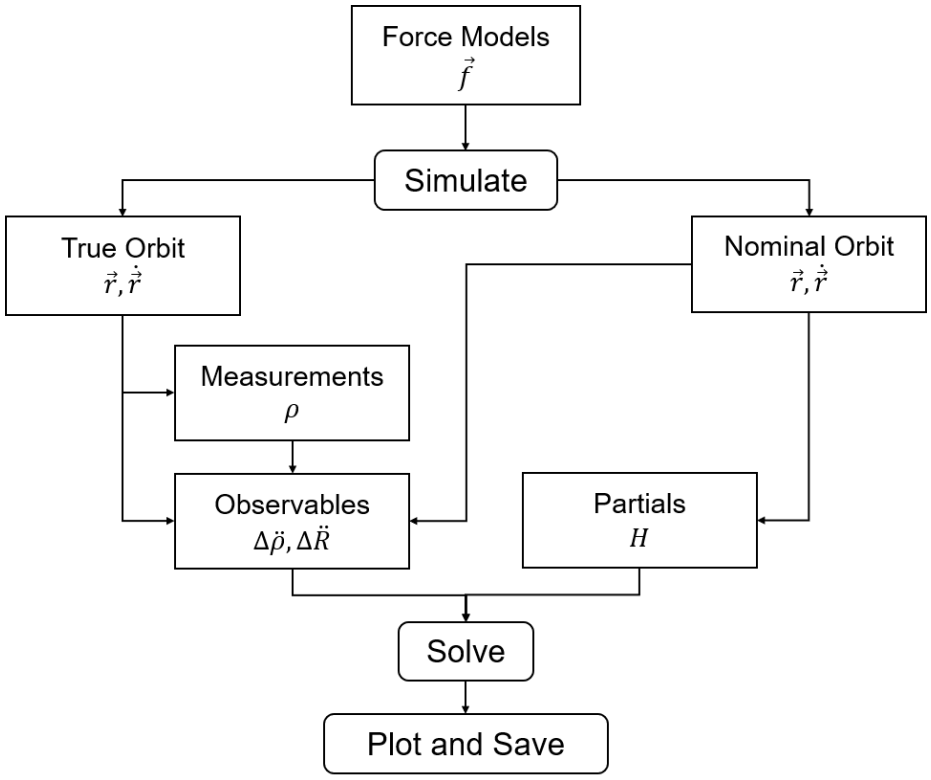

Figure 2.1: Structure of Simulation Implementation

are added onto the surface that are to be estimated later. The acting forces are therefore purely gravitational. In theory, if a pair of satellite is present, they would exert gravitational attraction on each other as well, but due to their low mass and comparatively similar distance to Earth, this effect can be neglected. Aerodynamic drag and solar radiation pressure, that usually act on any low-Earth orbit satellite, are also not included in the model.

While representing Earth as a point mass and ignoring drag may seem like an oversimplification of conditions, it should be noted that all these influences are usually modeled and/or estimated alongside any gravity field solution. While the observable generated in real life applications may contain additional influences, they could also be properly removed with the best of our knowledge. Thus, the difference between the two, commonly referred to as O(bserved)-C(omputed), will approximately remain the same. Therefore, omitting these gravitational anomalies in the first place enables the assessment of a best-case scenario. Specifically, the full geoid (the known collection of mean mass anomalies distributed over Earth's surface), drag and solar radiation pressure could be added as an additional acceleration to the simulation in (2.1).

The numerical integration of the equations of motion (2.2) is performed using the MATLAB function *ode45*, one day at a time (called an arc). The *ode45* integrator is an explicit, single-step solver, which means that it only needs the current state to calculate the best guess at the next time step (as opposed to needing data at multiple times). It is based on the Runge-Kutta family of integrators and can be expected to achieve up to nanometer precision in a two-body simulation where the analytic values at every time step can be computed with the Kepler equations (one day, 0.1 s step size) [10, Ch. 3.1]. While this precision may not be sufficient for scientific purposes using real data, it is acceptable for the simulation of a true orbit.

Nominal Orbit

Once the true orbit is generated and stored as a time series of position and velocity (for both satellites), this information can be corrupted with noise and then used as measurements to estimate the nominal orbit. This is a proxy for the more elaborate precise orbit determination done in practice. Because an orbit is fully defined by its initial conditions (given full knowledge of the acting forces), orbit determination methods reference any future state or measurement back to the initial time using State Transition Matrices (STMs). In the following, let

$$\vec{x}(t) = \begin{bmatrix} \vec{r} \\ \dot{\vec{r}} \end{bmatrix}$$

STMs Φ are solutions of the differential equation

$$\dot{\vec{x}}(t) = F\vec{x}(t)$$

that satisfy the relation

$$\vec{x}(t) = \Phi(t, t_0)\vec{x}(t_0)$$

For non-linear problems, where $\vec{x} = \vec{x}^* + \Delta\vec{x}$, $\dot{\vec{x}} = \dot{\vec{x}}^* + \Delta\dot{\vec{x}}$, and

$$\dot{\vec{x}}(t) = F(\vec{x}(t))$$

a first-order Taylor series expansion of $\vec{x}$ about the true trajectory $\vec{x}^*$ leads to the STM mapping the deviations back to the initial deviation:

$$\Delta\vec{x}(t) = \left[\frac{\partial\vec{x}(t)}{\partial\vec{x}(t_0)}\right]_{\vec{x}^*(t)} \Delta\vec{x}(t_0) = \Phi(t, t_0)\Delta\vec{x}(t_0)$$

Furthermore, a first-order Taylor series expansion of $\dot{\vec{x}}$ about $\vec{x}^*$ maps the deviation of the derivative to the current deviation of the state:

$$\Delta\dot{\vec{x}}(t) = \left[\frac{\partial F(\vec{x}(t))}{\partial \vec{x}(t)}\right]_{\vec{x}^*(t)} \Delta\vec{x}(t) = A(t)\Delta\vec{x}(t)$$

Combining the last two equations yields

$$\Delta\dot{\vec{x}}(t) = \dot{\Phi}(t,t_0)\Delta\vec{x}(t_0) = A(t)\Delta\vec{x}(t) = A(t)\Phi(t,t_0)\Delta\vec{x}(t_0)$$

Because $\Delta\vec{x}(t_0)$ is just a constant multiplier, the STM Φ can be numerically integrated using

$$\dot{\Phi}(t,t_0) = A(t)\Phi(t,t_0) \tag{2.19}$$

In practice, Φ is computed alongside the numerical integration of $\vec{x}$.

Using the STMs of the true orbit, a simple way to generate a nominal orbit is to estimate initial deviations to the true orbit using the state measurements of the true orbit. In order to generate an initial deviation in the first place, however, noise needs to be added to the measurements. Effectively, this reduces to estimating initial deviations from random noise:

$$\underbrace{\Phi(t,t_0)}_{6\times6}\underbrace{\Delta\vec{x}(t_0)}_{6\times1} = \underbrace{\vec{\eta}}_{6\times1}$$

In this work, Gaussian white noise with GRACE-typical uncertainties in the position and velocity is used:

$$\sigma_{\text{pos}} = 1 \text{ cm} \qquad\qquad \sigma_{\text{vel}} = 10 \text{ µm}$$

For observations at multiple time steps N_t, the STMs and noise vectors can be stacked

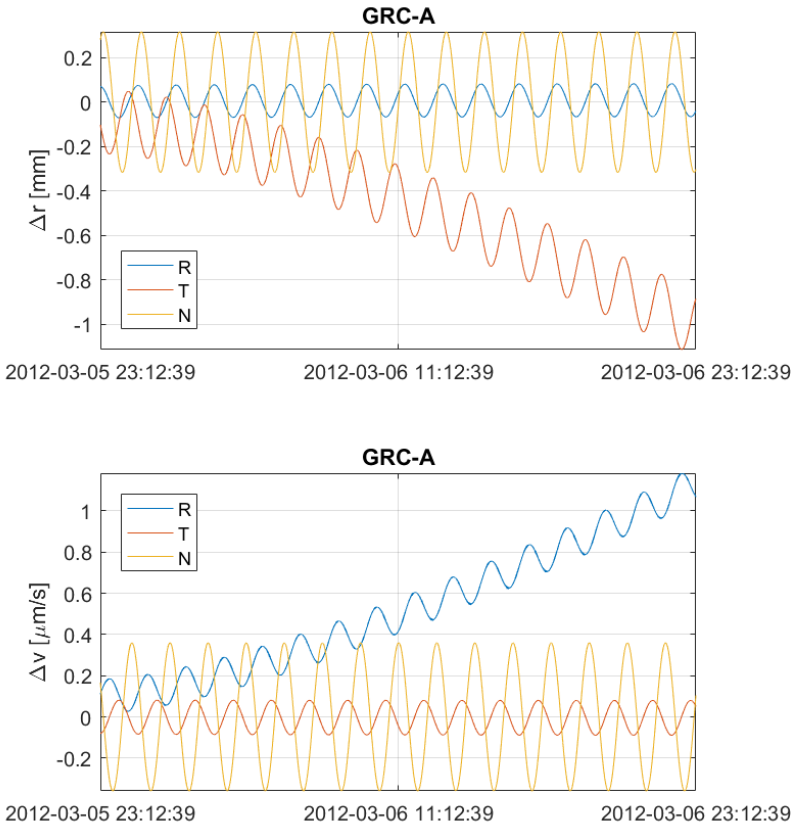

Figure 2.2: Differences between a true and simulated nominal orbit

to form the familiar

$$\underbrace{H}_{6N_t \times 6} \underbrace{\Delta\vec{x}(t_0)}_{6\times 1} = \underbrace{\vec{z}}_{6N_t \times 1} \tag{2.20}$$

Adding the estimated deviation to the true initial condition forms the perturbed initial conditions. Propagating them finally yields the simulated nominal orbit. This process is repeated on a daily basis.

Differences in the true and nominal orbit are usually presented in the Radial, Transversal and Normal (RTN) reference frame (see Appendix A.3). An example is shown in Figure 2.2. Secular and periodic trends are clearly visible over the time span of a day.

Measurements, Observables, and Partials

Using the true and nominal trajectories of both satellites, the equations derived in Section 2.2 can be used to generate measurements (i.e., what an instrument aboard the spacecraft would experience), observables (derived quantities used in the least squares formulation, the O-C) and partials (mapping the observable to the parameters to be estimated). Specifically,

- The inter-satellite range observations ρ, $\dot{\rho}$ and $\ddot{\rho}$ are generated with the true positions of the spacecraft (2.10), as this is what instruments (disregarding noise) would measure.

- The ideal, *analytic* observable $\Delta\ddot{\rho}$ as defined in (2.12) is calculated analytically using the true orbit and the knowledge of the mass of the anomalies present. It is used to verify and compare other quantities, and also serves to provide a best-case solution.

- $\Delta\ddot{R}^{\text{out}}$, analogous to (2.11) but substituting the true range, range rate and position with their nominal counterparts, and using numerical differentiation to compute the inter-satellite range acceleration, is the *simulated* observable. Because of the differentiation technique employed being a digital filter, it will also be referred to as the *filtered* observable. Using the nominal orbit implies that the filtered and analytic observables will not be equal.

- The partials H as defined in (2.15) are calculated with the nominal orbit.

To imitate the division of available GRACE observables into spatial grids covering Earth, and only accessing one grid at a time, a boundary is defined. A measurement is included in the solution process if at the time at which the measurement

is taken, at least one of the two satellites is above a rectangle defined by a margin in latitudinal and longitudinal direction centered at the modeled mass anomaly.

Least Squares Solution

Once orbits, measurements, observables and partials have been calculated for every time step, the linear system (2.16) can be solved using common least squares methods. A selection is given in [11, Ch. 12]. The most straightforward solution is given by solving the system's normal equation

$$(H^T H)\vec{x} = H^T \vec{z} \quad \Rightarrow \quad \vec{x} = (H^T H)^{-1} H^T \vec{z}$$

However, this method suffers from several drawbacks, namely

1. Suffering round-off errors when calculating $H^T H$, effectively a form of matrix squaring
2. Having to store the large $N_t \times N_t$ matrix $H^T H$ in memory
3. Inverting a large matrix, which is prone to numerical instabilities

To avoid these problems, the H matrix is usually decomposed and the solution equation rearranged. The most common method is the QR decomposition, where $H = QR$, Q is an orthonormal and R is an upper-triangular matrix [12, Ch. 2.4]. Defining

$$Q^T \vec{z} = \begin{bmatrix} \tilde{z} \\ \\ \tilde{\epsilon} \end{bmatrix}$$

and recognizing that

$$\min_{\vec{x}} \|H\vec{x} - \vec{z}\|^2 = \min_{\vec{x}} \|R\vec{x} - \tilde{z}\|^2 + \|\tilde{\epsilon}\|^2$$

the solution can be found by back-substituting for $\vec{x}$ in

$$R\vec{x} = \tilde{z}$$

Alternatively, the Singular Value Decomposition (SVD) can be used [13, Ch. 4]. The decomposition yields $H = U\Sigma V^T$, where Σ is purely diagonal (with the diagonal entries called singular values) and U, V are orthonormal. After rearranging, the solution of the system becomes

$$\vec{x} = V\ \Sigma^{-1}\ U^T\ \vec{z}$$

where it should be noted that Σ^{-1} is now just the inversion of each of the diagonal elements. Another positive side effect when using SVD is the introduction of singular values, which can be used as a metric of how numerically well-posed the system is. The condition number of a matrix is defined as the ratio of the largest to the smallest singular value, and the closer it is to one, the better. A high condition number implies that a small change in the observations can have an excessively large impact on the solution, making it very susceptible to noisy or imperfect observations.

In this work, SVD is used by default when estimating mass anomalies because of the variability in the condition numbers of H when experimenting with different mascon geometries and amplitudes. Although it is computationally more expensive, it is still only a fraction of time spent on propagating the orbits, which makes it

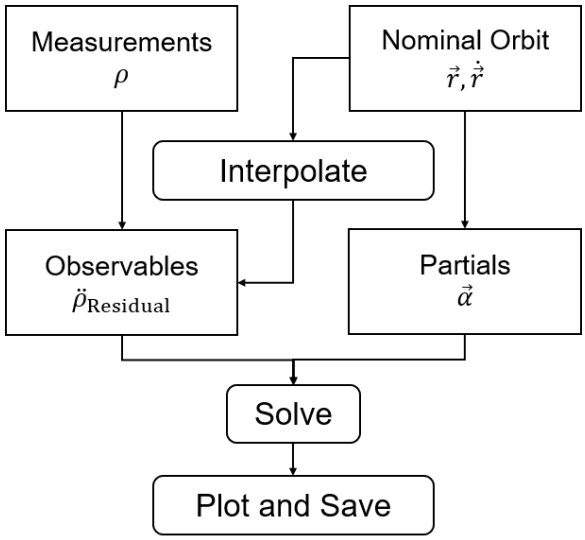

Figure 2.3: Structure of Estimation Implementation using GRACE Data

acceptable.

2.3.2 GRACE Data Analysis

In the second part of the work, instead of inferring mass anomalies that give rise to unmodeled accelerations, (2.18) will be used to estimate parameters of a model for their time variability, and determine if the force models are incomplete. A simplified structure of the implemented code is shown in Figure 2.3.

Editing Orbit

For GRACE and any other satellite missions, it is impossible to know the true orbit. GPS measurements enable real-time observation of the spacecraft's state. However, a significant factor in estimating the current position and velocity is the precision of the orbit of the GPS satellites, which are only approximate in real-time. After precise positioning orbits have been calculated (usually with a delay of approximately two weeks) for the GPS satellites, a new GRACE orbit can be estimated.

Using the combination of GPS measurements, satellite laser ranging (if available), accelerometers, and star trackers (the latter observations providing additional constraints on the state). The resulting orbit, called *editing* orbit in CSR nomenclature, is calculated iteratively by the CSR-internal Multi-Satellite Orbit Determination Program (MSODP) [14, Ch. 2]. A multitude of background models for influences such as the gravity field, atmospheric and oceanic tides, the ionosphere, and the troposphere are included. It is output at a 5 second rate, and the best estimate of GRACE's true orbit.

Measurements, Observables and Partials

The inter-satellite range measurement is performed using the K/Ka-Band Ranging (KBR) onboard system (see Section 3.1 and [15]). The micrometer-precision observations are then numerically differentiated to generate inter-satellite acceleration values $\ddot{\rho}_{\text{Observed}}$. One method to compute derivatives of discrete data is a CRN-class digital filter presented in Section 3.2. Because of the quality of the KBR instrument, $\ddot{\rho}_{\text{Observed}}$ is also the best approximation of the true range acceleration $\ddot{\rho}_{\text{True}}$ (after adjusting for necessary corrections).

The modeled acceleration $\ddot{\rho}_{\text{Modeled}}$ can be calculated numerically using (2.10) and all the available knowledge about the state of the spacecraft (e.g. attitude, orbit, mass), Earth's potential (influenced by solid, ocean and atmospheric tides) and other forces acting (e.g. solar radiation pressure, thruster activity). Alternatively, it can be numerically obtained using $\dot{\rho}_{\text{Modeled}}$, which, as well, can be calculated using all the available information present in the editing orbit.

As the understanding of the forces acting on the satellites increases, the residual $\ddot{\rho}_{\text{Residual}}$ between the true and modeled (O-C) acceleration is reduced. Apart from

intrinsic noise apparent in every physical process, it will contain the influence of any non-modeled force. Thus, analyzing the residual acceleration directly informs about the quality of the model. Any spatial or temporal pattern apparent in it is likely to be caused by either a real signal, or an incomplete understanding of instrument behavior or numeric corrections. Following the notation of Section 2.2 and (2.17), the residual acceleration becomes the observable

$$\ddot{\rho}_{\text{Residual}} = \ddot{\rho}_{\text{Observed}} - \ddot{\rho}_{\text{Modeled}} + \ddot{\rho}_{\text{Noise}}$$

Like in the orbit simulation case, a grid is then placed onto Earth's surface. Each observables is then associated with a grid element if at the time of the measurement, at least one of the two satellites is above it.

Least Squares Solution

Collecting all the measurements and partials for each grid element and stacking them over time yields enough data to estimate potential patterns using (2.18) and standard least squares methods on a grid-by-grid basis. In contrast to estimating masses, fitting simple polynomial and periodic coefficients to a time series is much less ill-posed. Therefore, the QR decomposition (as presented in Subsection 2.3.1) is used to solve the linear system without loss of precision.

Chapter 3

GRACE Ranging Products

This chapter serves to illustrate how inter-satellite range acceleration (as needed in the least squares formulation) is obtained from either the ranging instrument aboard each spacecraft, or the ground-processed orbit solutions. Section 3.1 briefly presents the phase measurement as output by the satellite's instruments. The numerical differentiation method, a digital filter simultaneously reducing signal noise, is presented in Section 3.2. Its performance is then assessed in Section 3.3 for both simulation and data analysis parts.

3.1 Range Measurement

The distance between the spacecraft can be calculated through the time of flight of the microwave signals exchanged between the two. However, the phase measurements are inherently corrupted by oscillator noise and time tag errors. To address these issues, dual one-way ranging (DOWR) is used, where phase measurements from both satellites are combined in ground processing. To correct for the ionospheric delay, DOWR is performed on both K (26 GHz) and Ka (32 GHz) band frequencies at a 10 Hz output rate. The result is the range measurement, precise to micrometers, and only offset by a constant bias [15, Ch. 2.2]. Using GPS data, this bias can be estimated, although it is not necessary for the generation of inter-satellite range acceleration. In reference to the notation used in Section 2.2 and specifically to the

definition of ρ_i in (2.10):

$$\rho_i = R_i^{\text{raw}} + R^{\text{bias}} \tag{3.1}$$

3.2 Acceleration Filtering

To suppress noise outside of the signal band, and generate the range derivatives, a digital filter was developed [16, App. A.3]. The signal band is defined by the frequency spectrum where the gravity signal in the data can be found. For GRACE, the goal is to estimate the global gravity field to spherical harmonics up to degree 200, which corresponds to a frequency of 0.036 Hz. For a target output sample rate of 0.2 Hz, the corresponding Nyquist frequency of 0.1 Hz leaves enough margin for this, and is therefore chosen to be the target bandwidth for the low-pass filter.

The perfect low-pass filter is a rectangular window in the frequency domain, and corresponds to the sinc function in the time domain. Because sinc has an infinite support, however, such a filter is impossible to implement in reality, and a window needs to applied to reduce its range. A purely rectangular window in the time domain would suffice, but entails defects in the frequency domain due to its sharp edges. To mitigate these problems, a window with smoother transitions can be chosen. For GRACE, a CRN filter is used: N self-convolutions of a rectangular time-domain window. This filter class has a simple closed-form solution in both the time and frequency domain, is highly customizable, and can be designed in discrete time. To generate time derivatives of the observable, the weighting function is differentiated in the frequency domain, as differentiation becomes multiplication. The resulting filter (as summarized in [17, App. B] and used in GRACE processing) is shown in (3.2),

where i is the time index of the measurements.

$$R_i^{\text{out}} = \sum_{n=-N_h}^{N_h} F_n R_{i-n}^{\text{raw}} \qquad F_n = \frac{1}{F^{\text{Norm}}} \sum_{k=-N_h}^{N_h} H_k \cos\left(\frac{2\pi kn}{N_f}\right) \tag{3.2a}$$

$$\dot{R}_i^{\text{out}} = \sum_{n=-N_h}^{N_h} \dot{F}_n R_{i-n}^{\text{raw}} \qquad \dot{F}_n = \frac{1}{F^{\text{Norm}}} \sum_{k=-N_h}^{N_h} -(2\pi k/T_f)\, H_k \sin\left(\frac{2\pi kn}{N_f}\right) \tag{3.2b}$$

$$\ddot{R}_i^{\text{out}} = \sum_{n=-N_h}^{N_h} \ddot{F}_n R_{i-n}^{\text{raw}} \qquad \ddot{F}_n = \frac{1}{F^{\text{Norm}}} \sum_{k=-N_h}^{N_h} -(2\pi k/T_f)^2\, H_k \cos\left(\frac{2\pi kn}{N_f}\right) \tag{3.2c}$$

where $N_h = (N_f - 1)/2$ and

$$H_k = \sum_{m=-N_B}^{N_B} \left(\frac{\sin\left(\pi(k-m)/N_c\right)}{\sin\left(\pi(k-m)/N_f\right)}\right)^{N_c} \tag{3.2d}$$

$$F^{\text{Norm}} = \sum_{i=-N_h}^{N_h} \left(\cos\left(\frac{2\pi f_0 i}{f_s}\right) \sum_{k=-N_h}^{N_h} H_k \cos\left(\frac{2\pi ki}{N_f}\right)\right) \tag{3.2e}$$

Sample values for standard GRACE processing are shown in Table 3.1. Note the

f_s	= raw sampling rate	= 10 Hz
f_0	= dominant signal frequency	= 0.37 mHz
B_t	= target low-pass bandwidth	= 0.1 Hz
T_f	= filter window length	= 70.7 s
N_c	= number of self-convolutions	= 7
N_R	= number of points in basis rectangle	= 101
$N_B = BT_f$	= number of frequency bins	= 7
$N_f = f_s T_f = N_c N_R$	= number of points in filter window (odd)	= 707

Table 3.1: Standard CRN Parameters for GRACE

difference between the ideal (target) bandwidth B_t, and the effective (quantized) bandwidth as specified by $B = N_B/T_f \approx 0.0099$ Hz. Similarly, the effective filter time span T_f is derived from an ideal time span T, but sufficing the requirements of the integer nature of its relations to N_c, N_R and N_B.

For GRACE processing, the filtering of the range includes another, purely numerical step [17, Ch. 2.3.4]. Before applying the filter to the raw range measurements, a simple quadratic is fit through the data points in the filter window, and removed. Only the residual is filtered. The final range value is then the filtered residual combined with the middle point of the removed quadratic.

Now that a numerical way of calculating the inter-satellite range acceleration is known, the filtered observable as introduced in Subsection 2.3.1 can finally be defined. Connecting (3.2) to the definition of ρ_i (2.10), recognizing that the constant bias of R^{raw}_{i-n} is irrelevant to the calculation of derivatives, and neglecting noise, the filtered inter-satellite range acceleration is given by:

$$\ddot{\rho}_i \approx \ddot{R}^{\text{out}}_i = \sum_{n=-N_h}^{N_h} \ddot{F}_n R^{\text{raw}}_{i-n} = \sum_{n=-N_h}^{N_h} \ddot{F}_n \rho_{i-n} \tag{3.3}$$

The filtered observable can now be defined as:

$$\Delta\ddot{R}^{\text{out}} = \ddot{R}^{\text{out}} - \frac{1}{\rho}\left(\|\dot{\vec{\rho}}\|^2 - \dot{\rho}^2\right) - Gm_0\hat{r}^T\left(\frac{\hat{r}_{0A}}{r^2_{0A}} - \frac{\hat{r}_{0B}}{r^2_{0B}}\right) \tag{3.4}$$

where the nominal orbit needs to be used to calculate the second and third term.

3.3 CRN Filter Performance

To validate the implementation of the filter, a comparison is made between official Level 1B filtered GRACE inter-satellite biased range and range acceleration, and processed results obtained from the raw, 10 Hz biased DOWR range. Figure 3.1 shows that, for an arbitrary day, the CRN filter presented above does yield the same results as the official GRACE data repository (to machine precision).

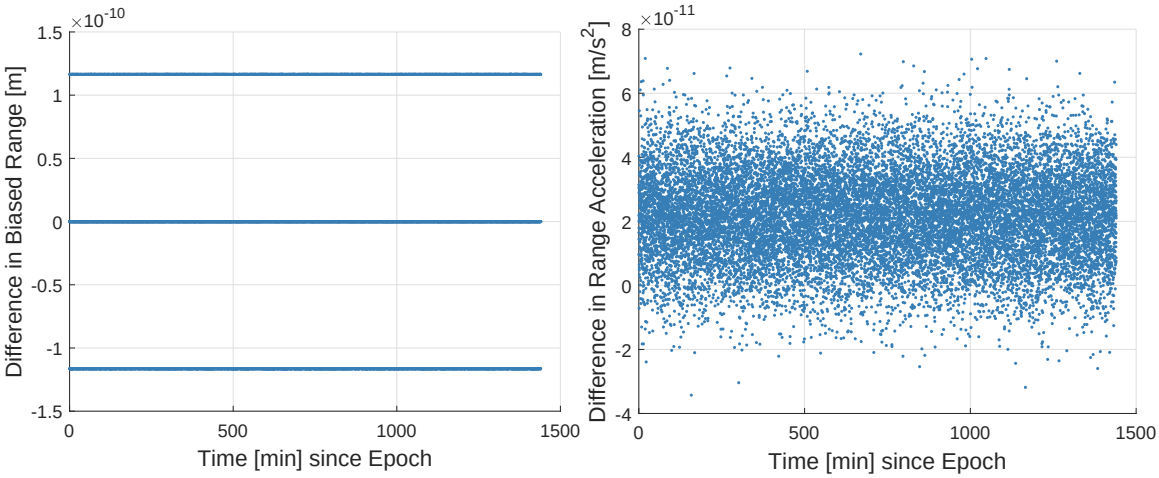

(a) Biased Range

(b) Range Acceleration

Figure 3.1: CRN Filter Validation

In the following, the CRN filter is used to numerically differentiate a variety of input data to assess its performance with respect to the two main goals of this study: generating the range acceleration to infer mass anomalies using a simulated orbit; and generating range acceleration residuals to create global maps of unmodeled influences.

3.3.1 Using Simulated Orbits

Recalling the estimation formulation in Section 2.2, to estimate the parameters of a time-varying mass anomaly, we need the inter-satellite range acceleration $\ddot{\rho}$ to form the observable $\Delta\ddot{\rho}$, see (2.11). In this section, the goal is to use a simulated, true orbit to compare the true range acceleration as calculated by the right-hand side in (2.10c) to the output of the CRN filter (3.2c). The following plots are generated using a 10 year-long simulated mission, with one mass anomaly present (exhibiting a linear trend and 8 different periodic frequencies) and without any added observation noise.

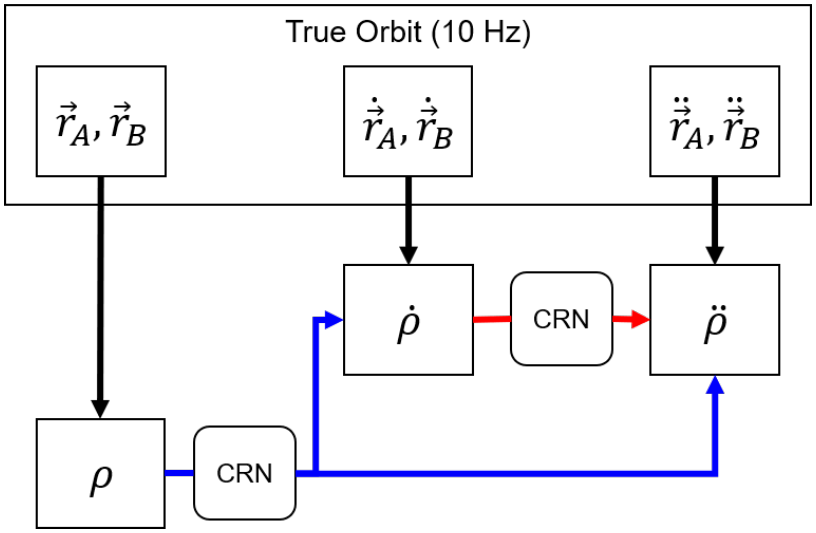

Figure 3.2: Relations Between Observables in the case of a Simulated Orbit. The color coding here is reflected in Figures 3.3 through 3.6.

Figure 3.2 provides an overview of the quantities compared in this section. In reality, our measurements of the biased range between the spacecraft is very precise. When taking derivatives, the bias is irrelevant, and we can therefore use the true range as the input for our CRN filter differentiation routine in order to simulate real mission behavior. To further test the performance of the numeric derivatives, we can reduce the differentiation order of the CRN filter (3.2) when generating range acceleration if we use the true range rate as an input. Then, we can use the expression for the first derivative ($\dot{F}_n$ instead of $\ddot{F}_n$), but get the same physical quantity.

Figure 3.3 compares the true range to the smoothed range as output by the zeroth order of the CRN filter, for two different days of the baseline simulation: the first day, which features a direct pass of the satellites over the mass anomaly, and a day 5 years into the mission, also featuring a pass over the anomaly. These two days will be used throughout this subsection. Figure 3.4 compares the corresponding range accelerations.

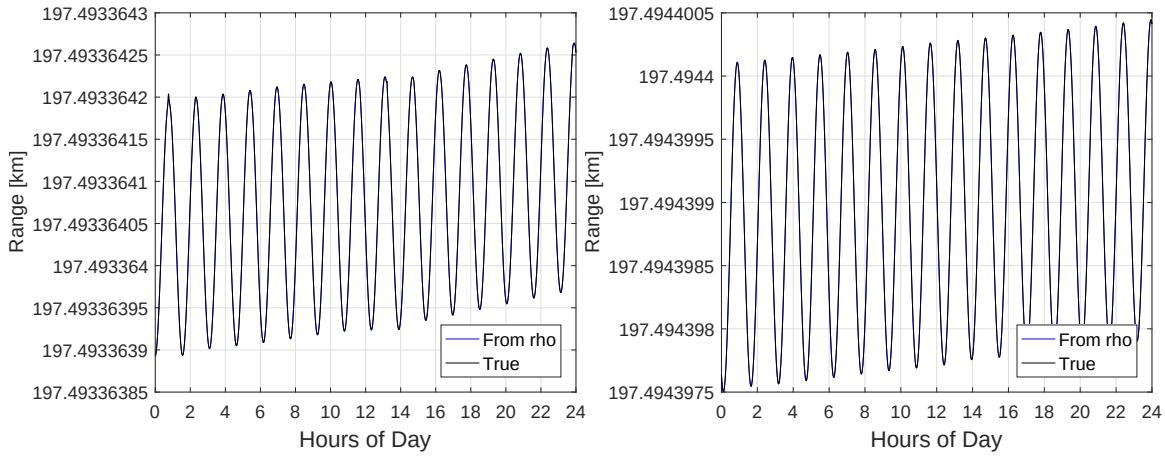

(a) Total, Day 1

(b) Total, Day 1824

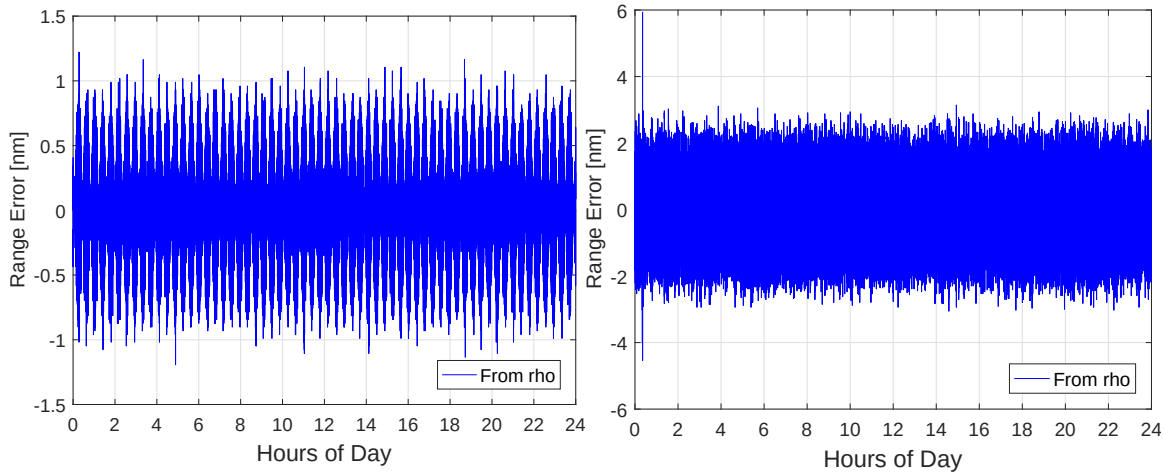

(c) Error, Day 1

(d) Error, Day 1824

Figure 3.3: CRN Range Results for Simulated Orbit. The error is defined relative to the true range.

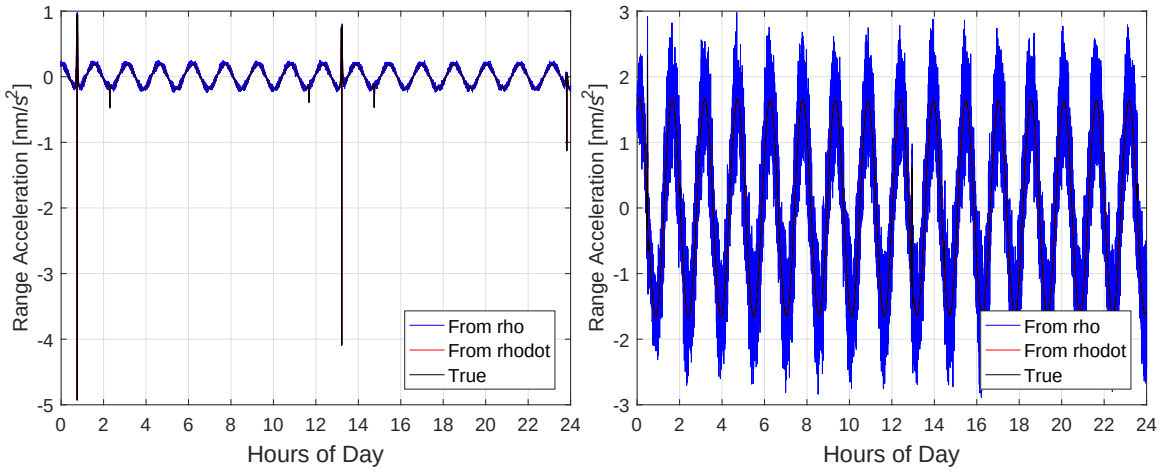

(a) Total, Day 1

(b) Total, Day 1824

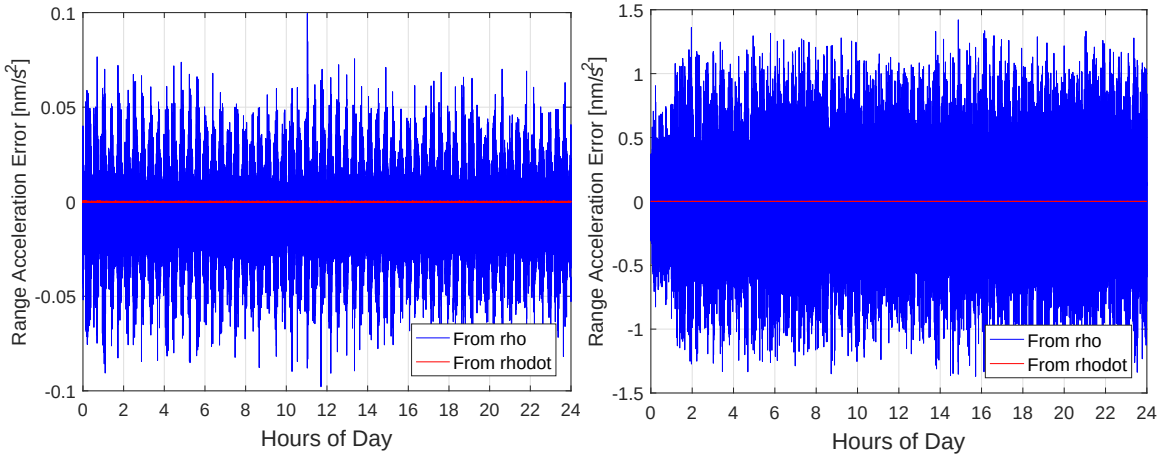

(c) Error, Day 1

(d) Error, Day 1824

Figure 3.4: CRN Range Acceleration Results for a Simulated Orbit. The error is defined relative to the true range acceleration. The numerically derived values are given for the cases where the CRN filter is applied twice (generating acceleration from range ρ) and once (generating acceleration from range rate $\dot{\rho}$).

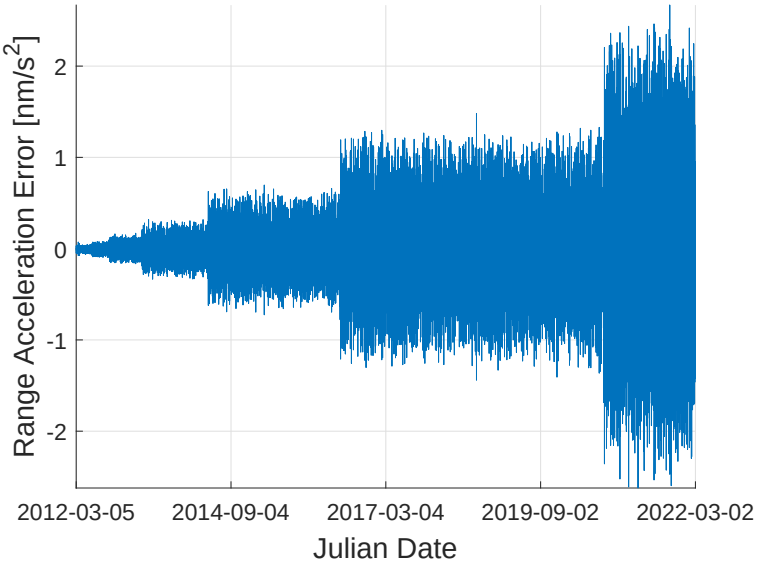

Figure 3.5: Difference between Analytical and Filtered Range Acceleration

In general, we can see the filter working as expected. Both numerically-derived range accelerations (twice-differentiated from ρ, or once-differentiated from $\dot{\rho}$) track the true range acceleration with an error on the nanometer-per-second-squared scale (which is comparable to the accepted noise levels of GRACE of about 2 nm/s^2). The next thing to note, however, is that the error in both range and range acceleration estimates deteriorate over time. Figure 3.5 confirms this behavior for the whole 10 year simulation time span.

Plots of the power spectral density (PSD) (Figure 3.6) of the three range acceleration observables indicate that high-frequency noise is introduced inside the passband of the filter, especially in the case of differentiating twice. Additionally, the magnitude of the introduced error close to the cutoff frequency increases between the two dates. Using the range rate as the input and only differentiating once reduces the error significantly by orders of magnitudes.

The large and growing errors are therefore most likely due to the quality of the

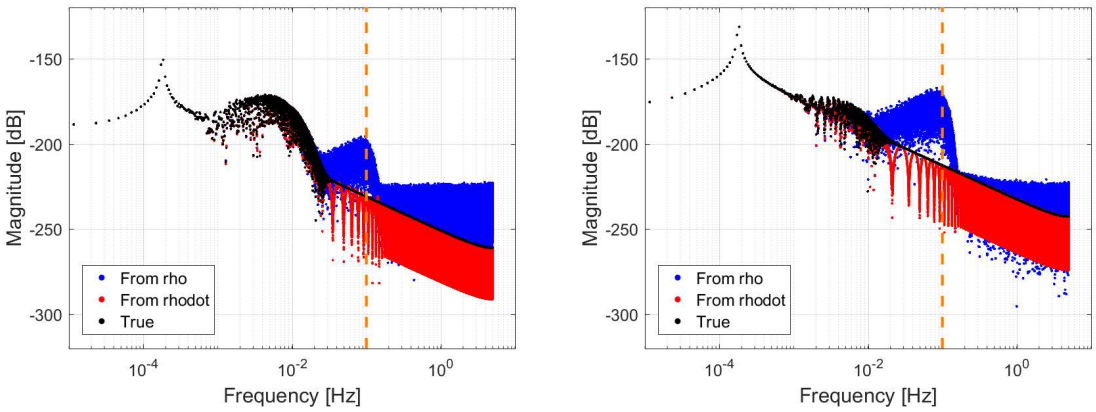

(a) Day 1 (b) Day 1824

Figure 3.6: Power Spectral Density of $\ddot{\rho}$ for a Simulated Orbit. The CRN filter bandwidth is marked in orange.

orbit propagator and subsequent round-off errors. As alluded to in Subsection 2.3.1 and discussed in detail by [10, Ch. 3], the simple, Matlab-included *ode45* function is not comparable to the integrators used for research-quality results. Apparently, the second-order CRN differentiating coefficients are significantly more sensitive to these errors from a numerical standpoint. Additionally, because the daily orbit propagation relies on the last state of the previous arc to be initialized, the accumulation of errors is significant for a total simulation time span of 10 years, explaining the increase in total noise level between the two dates.

Reducing the target bandwidth of the CRN filter only shifts the problem. While smaller values for B_t reduce the average range acceleration error, it drastically increases the errors when the satellites pass over the anomaly, and the excess acceleration due to the anomaly is the highest, see Figure 3.7. This is particularly harmful for the estimation process, as these are the times where observables have the highest influence on the solution.

For both of the aforementioned reasons, the interpretation of results using

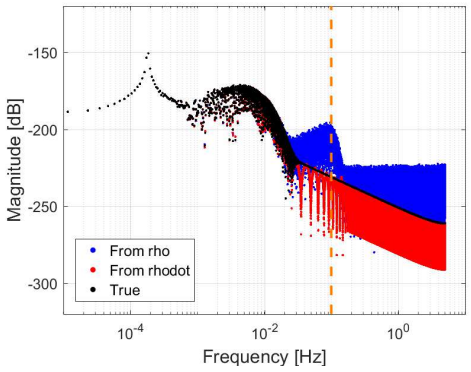

(a) PSD

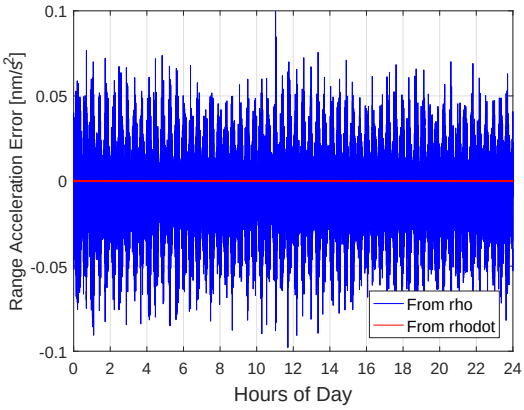

(b) Range Acceleration Error

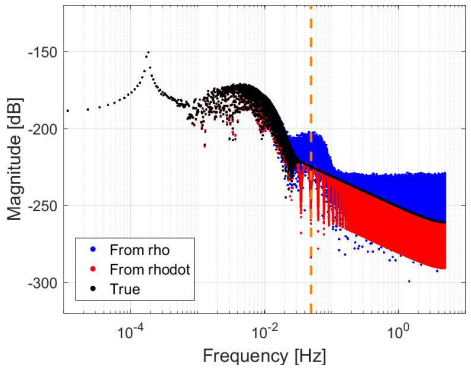

(c) PSD

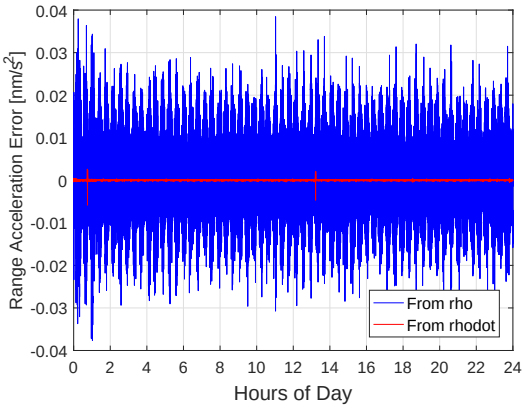

(d) Range Acceleration Error

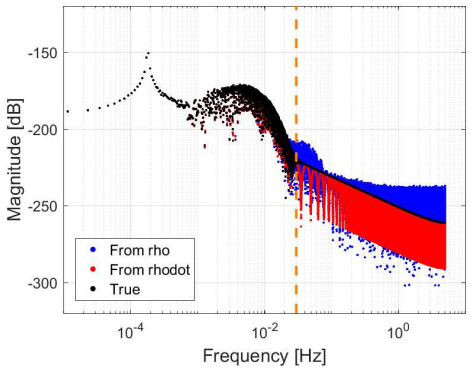

(e) PSD

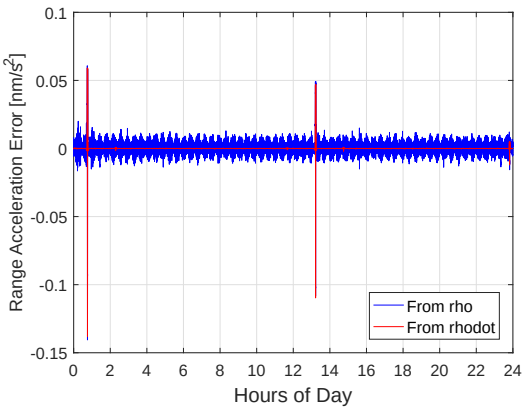

(f) Range Acceleration Error

Figure 3.7: CRN Range Acceleration Behavior for Different Bandwidths. *Top:* $B_t = 0.1$ Hz, *Center:* $B_t = 0.05$ Hz, *Bottom:* $B_t = 0.03$ Hz

simulated orbits in the rest of this study will focus on the cases where the true range acceleration is used as the observable.

3.3.2 Using Interpolated GRACE Data

In the second part of the work, the goal is to calculate range acceleration residuals between the observed and modeled accelerations experienced by GRACE, as introduced in (2.17). The residuals can then be used to fit a model (such as the one used for the mass time series) through them to search for unmodeled forces, see (2.18). Although there is no knowledge of the true inter-satellite range, the precise measurements of the KBR instrument can be assumed to be the closest possible, and therefore the best approximation of the true range acceleration is computed by twice-differentiating the KBR measurements.

Our best estimate of GRACE's orbit is given by the editing orbit as presented in Subsection 2.3.2. It contains the information of all knowledge available: Earth's gravity field (including monthly variations), oceanic, atmospheric and solid tides, as well as attitude and GPS measurements [18]. It is stored in the form of 5 s pairs of position and velocity for both spacecraft. If we want to compute the residual acceleration at each 10 Hz time step, one straightforward way of doing so is to interpolate the editing orbit to match the KBR's output frequency, and using the CRN filter calculate the modeled acceleration given the range (or range rate) as implied by the satellites' states. Table 3.2 provides an overview of the available data and derivable quantities, and Figure 3.8 sketches the relations between them. Appendix A.1 describes the Hermite interpolation technique used.

As Figure 3.9 through Figure 3.12 show for the time span of an arbitrary day, the interpolation works as expected, and provides CRN-filtered range, range rate

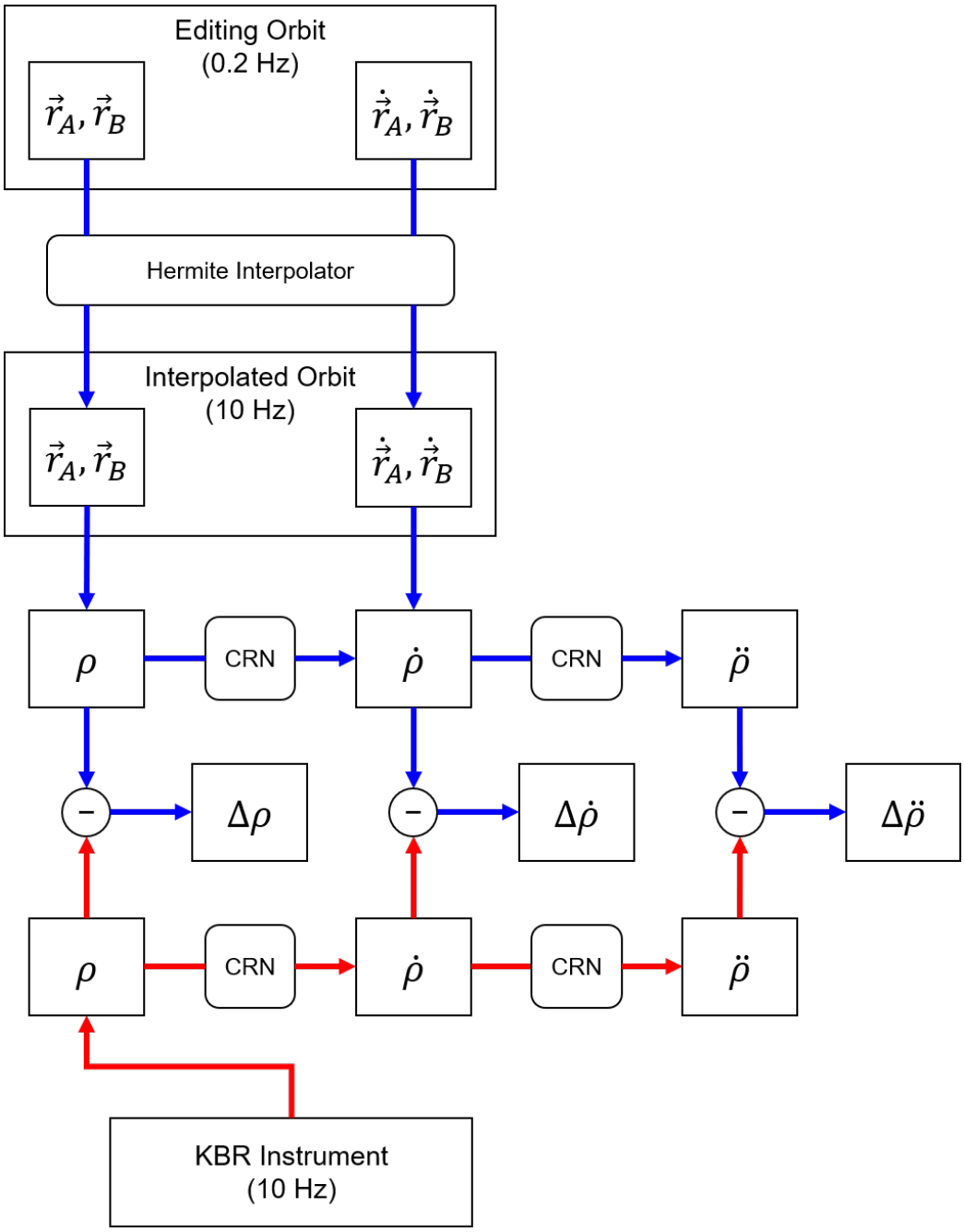

Figure 3.8: Relations Between Observables in the case of Interpolated GRACE Data. The color coding here is reflected in Figures 3.9 through 3.13.

Type	Rate	$\vec{r}$	$\dot{\vec{r}}$	ρ	$\dot{\rho}$	$\ddot{\rho}$
Editing Orbit	0.2 Hz	●	●	●	●	
Interpolated Editing Orbit	10 Hz	●	●	●	●	◑
KBR Observations	10 Hz			●	○	○

Table 3.2: Overview of Interpolated and Differentiated Orbit and Measurement Products. ●: Quantity is either explicitly stored in the product, or can be derived analytically, ◗: Range Acceleration based on interpolated orbits has to be derived using either the interpolator's analytic expression, or using the CRN filter (as it is done in this study), ○: Range Rate and Acceleration based on the KBR observations has to be derived using the CRN filter.

and range acceleration time series close to the measured ones. The range acceleration generated using range (and twice differentiating) and using range rate (differentiating once) yield practically the same result. Their power spectral densities are shown in Figure 3.13 (blue)—all of their PSDs overlap. Furthermore, they exhibit an increase of the noise level in the higher frequencies similar to the simulated results shown in Figure 3.6.The higher power at lower frequencies is most likely due to the information that got "added" by means of the interpolation, to make use of the 10 Hz data—it is not a physical signal.

As a comparison, the PSD of the official range acceleration residuals (0.2 Hz sampling rate) is shown in the same figure (green). It has approximately the same signal power in the band between 0.5 mHz and 10 mHz, but does not show any of the noise influences presented above.

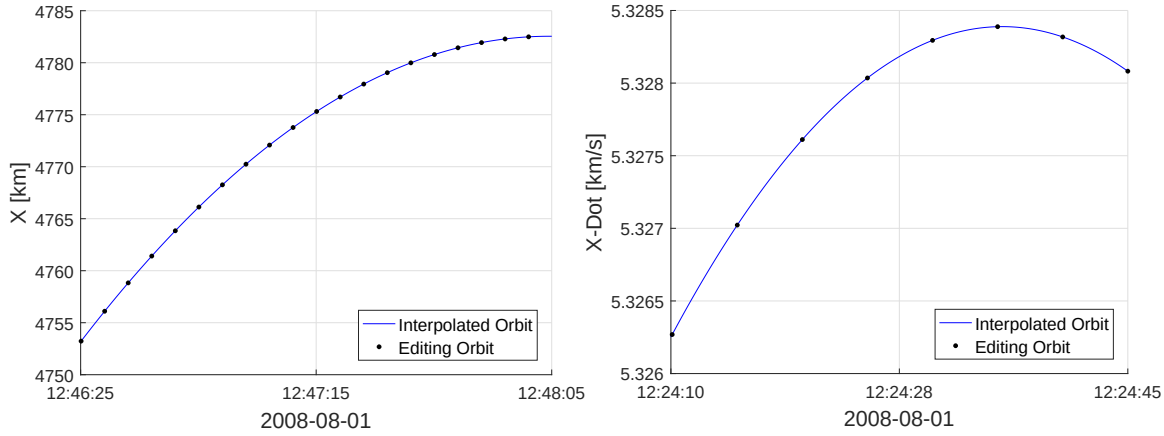

(a) Position X (b) Velocity $\dot{X}$

Figure 3.9: Orbit Interpolation Performance (along the ECI x-axis)

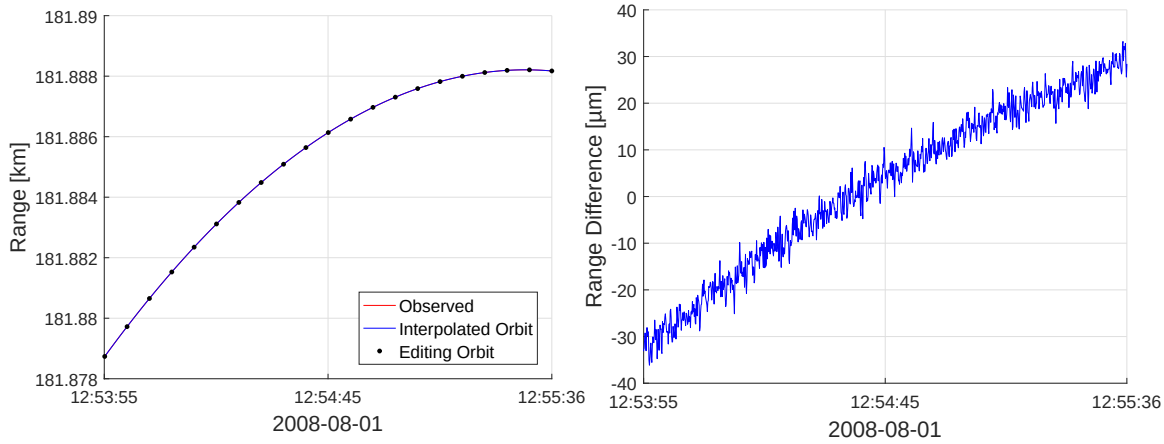

(a) Range ρ (b) Range Difference $\Delta\rho$

Figure 3.10: Range Interpolation Performance.

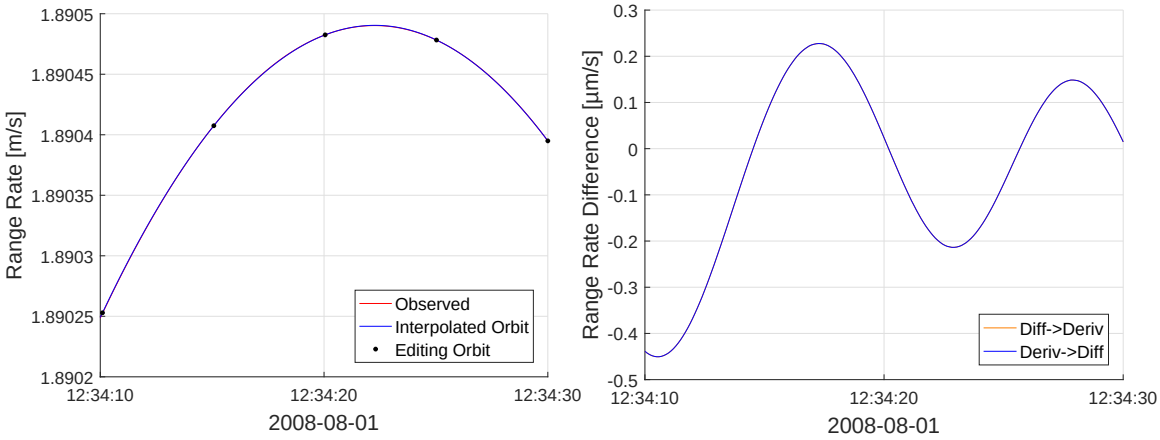

(a) Range Rate $\dot{\rho}$ (b) Range Rate Difference $\Delta\dot{\rho}$

Figure 3.11: Range Rate Interpolation Performance. The orders in which the differencing and derivatives are taken are shown in the legend.

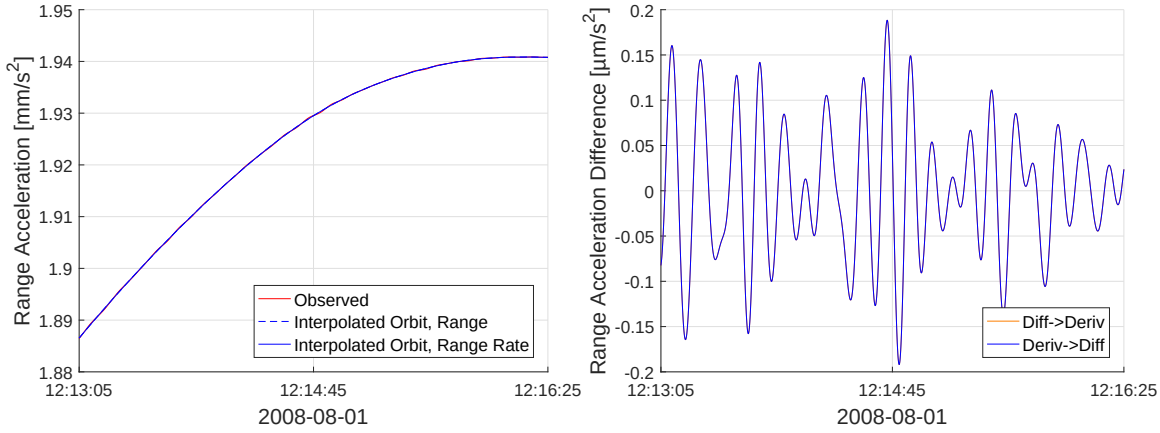

(a) Range Acceleration $\ddot{\rho}$ (b) Range Acceleration Difference $\Delta\ddot{\rho}$

Figure 3.12: Range Acceleration Interpolation Performance. The orders in which the differencing and derivatives are taken are shown in the legend.

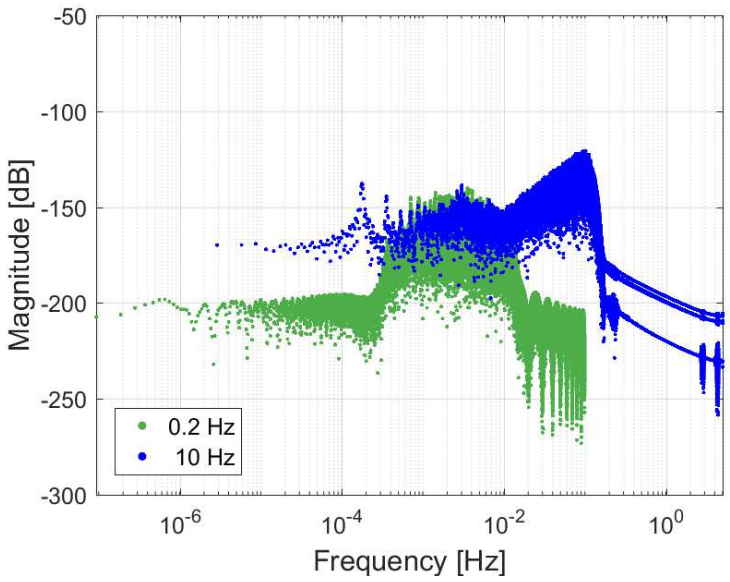

Figure 3.13: Comparison of Range Acceleration Power Spectral Densities. The CRN filter bandwidth is $B_t = 0.1$ Hz.

Chapter 4

Results

This chapter presents, explains and analyzes the results from the two key parts of this study:

- Assessing the feasibility of using spatially gridded range accelerations to infer mass anomalies present in the respective region. This work is performed using simulations of GRACE-like orbits under the attraction of a spherical Earth and a single mass anomaly, positioned on the Earth's surface.
- Searching for unmodeled accelerations as experienced by the GRACE satellites during their mission span using the KBR measurements and best available orbits.

First, a common model for tides is presented and explained in Section 4.1. It fits the mathematical framework developed in Section 2.2, which is used as the general form of an unmodeled mass or acceleration. In Section 4.2, the main findings of the simulations are presented. A sensitivity analysis is performed in Subsection 4.2.3 to assess parameter influences. Finally, estimated residual accelerations in GRACE data are shown in Section 4.3 as a first step to identify local unmodeled mass anomalies.

4.1 Tidal Theory

The earliest known connection between sea tides and the Moon by humankind dates back to the 4^{th} century BC [19]. Since then, significant insights into understanding gravitational attraction and the tide-generating potential were published by

Kepler, Newton and Laplace. However, it was not until the Fourier analysis was applied to the theory in the late 18^{th} and early 19^{th} century that different tidal frequency could be distinguished and accurate predictions could be made. A scheme to categorize and describe specific harmonic constituents developed by Arthur T. Doodson in 1921, now called Doodson numbers, is still in use [20].

In the modern context, tides can refer to a multitude of oceanic, atmospheric, and solid Earth periodic oscillations. In this work, only oceanic tides expressed as excess or default mass (or equivalent sea surface height) are considered. Given a set of elemental frequencies, amplitudes and phases, the total tide can be calculated by superimposing every constituent (synthesis). In return, given direct or indirect observations such as sea level or gravitational anomalies, the underlying constituents can be inferred (analysis).

The model of a time-varying mass in Section 2.2 already included such a formulation. In fact, if the phases θ_l in (2.13) are calculated with tidal harmonic frequencies, and a_l, b_l are their respective amplitudes, the periodic part of a mass variability due to tidal height change is completely described:

$$f_{Periodic} = \sum_{l=1}^{N_c} a_l \sin\theta_l + b_l \cos\theta_l$$

The constituent frequencies are multiples of several fundamental frequencies that give rise to the tides, such as the Moon's orbit around Earth, or Earth's movement around the sun. The International Astronomical Union has specified conventions to calculate key angles between the bodies. The phases for each tidal constituent l can then be generated by multiplying six independent angles ϕ_r with the six tide-specific integer

Doodson coefficients $d_r^{(l)}$ [20, 21]:

$$\theta_l = \sum_{r=1}^{6} d_r^{(l)} \phi_r \tag{4.1}$$

The independent angles, using Doodson's notation, are chosen to be

$\phi_1 = \tau$	Local mean lunar time angle
$\phi_2 = s$	Moon's mean longitude
$\phi_3 = h$	Sun's mean longitude
$\phi_4 = p$	Longitude of Moon's perigee
$\phi_5 = N'$	Negative longitude of Moon's mean node
$\phi_6 = p_1$	Longitude of Sun's mean perigee

The coefficients $d_r^{(l)}$ for eight major tidal species are given in Table 4.1. Doodson recognized that the first coefficient is always positive, and the vast majority of coefficients $r = 2 \ldots 6$ are between -4 and 4. In his paper, he therefore introduced a compact notation by adding 5 to the last five coefficients, and calling the resulting number sequence the *argument-number*, which today is just called Doodson number. The constituent's symbols follow George Darwin's notation from the early 20^{th} century.

Finally, it should be noted that in reality, the amplitudes of the constituents change as Earth's distance and orientation to the Moon and Sun varies over the course of its orbit. These effects are neglected for the simulations and the amplitudes are set to be constant.

Species l	Symbol	Coefficients $d_r^{(l)}$						Number
Lunar diurnal	K_1	1	1	0	0	0	0	165.555
Lunar diurnal	O_1	1	-1	0	0	0	0	145.555
Larger lunar elliptic diurnal	Q_1	1	-2	0	1	0	0	135.655
Solar diurnal	P_1	1	1	-2	0	0	0	163.555
Principal lunar semidiurnal	M_2	2	0	0	0	0	0	255.555
Principal solar semidiurnal	S_2	2	2	-2	0	0	0	273.555
Larger lunar elliptic semidiurnal	N_2	2	-1	0	1	0	0	245.655
Lunisolar semidiurnal	K_2	2	2	0	0	0	0	275.555

Table 4.1: Doodson numbers of eight major tidal constituents

4.2 Estimating Local Tides Using Simulated Orbits

Using the framework developed in Chapter 2, the tidal modeling of Section 4.1, and optionally the filtering presented in Section 3.2, simulations can be run to assess the errors in the estimation of mass variations using regionally restricted observations. First, simulation characteristics are presented that enable meaningful comparisons of different runs. Then, a baseline case is discussed.

4.2.1 Characterizing a Simulation

The following criteria are used to describe the nature of the simulation, as well as interpret their accuracy.

Setup

- **Mass Variability Function.** The type of function that defines how the mass of the included anomalies varies over time. In most cases, it consists of a polynomial and a periodic term (2.13).
- **Number and Positions of Mascons.** The spatial arrangement of the mascons, defined by pairs of latitude and longitude, has an influence of the ability

to estimate the individual effects.

- **Regional Restriction.** Defines whether only measurements close to the mascons, or the entire set of observations are used. Can include the specific latitudinal and longitudinal margins.

- **Simulation Length.** Time span used in the simulation. Short (days to months) for testing purposes, long (multiple years) otherwise to resolve aliases.

- **Filter Parameters.** Describes the type of filter used (usually a CRN-class one), and applicable parameters (e.g., for a CRN filter, number of convolutions or target bandwidth).

Performance

- **Condition Number.** The condition number of the mapping matrix H, see (2.16), is an indicator of how numerically well-posed the problem is. The closer the condition number is to one, the better, see Subsection 2.3.1.

- **Mass RMSE.** The Root-Mean-Squared Error of the Mass is defined for each mascon j as

$$\mathrm{RMSE}^{\mathrm{Mass}} = \sqrt{\frac{1}{N_t}\sum_{m=1}^{N_t}(M_m^t - M_m^e)^2}$$

where the M_m^t is the true mass of the mascon at time index m as defined by the parameters $\vec{\beta}$, and M_m^e is the estimated mass, calculated using the solution of the least squares problem (2.15). It is independent from the underlying mass variability function. It will be different depending on which observable (analytic or filtered) is used.

- **Observable RMSE.** The Root-Mean-Squared Error of the observable is defined as

$$\mathrm{RMSE}^{\mathrm{Observable}} = \sqrt{\frac{1}{N_t}\sum_{m=1}^{N_t}\left(\Delta\ddot{R}_m^{\mathrm{out}} - \Delta\ddot{\rho}_m\right)^2}$$

  where $\Delta\ddot{R}_m^{\mathrm{out}}$ (3.4) is the filtered observable (using measurements derived from the true orbit, and corrective terms derived from the nominal orbit) and $\Delta\ddot{\rho}_m$ (2.12) is the analytic observable, calculated from the true orbit. It is useful to assess the difference between the analytic, true observable and the observable that a practical filter relying on measurements and nominal orbits can create.

- **Filter RMSE.** The Root-Mean-Squared Error of the filter $\mathrm{RMSE}^{\mathrm{Filter}}$ is defined just as $\mathrm{RMSE}^{\mathrm{Observable}}$, with the only difference that the corrective terms are also derived from the true orbit, which makes it dependent only on the filter's performance.

4.2.2 Results of the Baseline Simulation

The parameters of the baseline simulation are shown in Table 4.2 (the same simulation was used as the basis for Subsection 3.3.1). A time span of 10 years ensures that any aliasing between the periodic constituents can theoretically be resolved. The epoch is chosen arbitrary and irrelevant to the simulation. An instrument sampling and orbit output frequency of 0.2 Hz is adopted from the GRACE mission. To assess the digital filter's performance, filtered observables are generated alongside the analytic ones, and use default GRACE CRN filter parameters.

The selection of coefficients for the mass variability functions of the mass anomaly abstracts the motivating example of Greenland's fjords. A mass anomaly is placed at the center of Scoresby Sound (Figure 4.1), with its maximum amplitude

Time Span	10 y
Epoch	2012-03-05 23:12:40
Sampling Frequency	0.1 Hz
Types of Orbits	True and Nominal
Types of Observations	Analytic and Filtered
Filter Type	CRN
Filter Parameters	$N_c = 7$ $B_t = 0.1$ Hz $T_f = 70.7$ s
Number of Mascons	1
Position of Mascons	Lat = 70.8 deg, Lon = 335.2 deg
Size of Region	ΔLat = $\pm$4 deg ΔLon = $\pm$3 deg
Polynomial Coefficients	Constant 0 t Linear 225.0 Mt/y
Periodic Constituents	K_1 0.94 Gt 0.94 Gt O_1 0.88 Gt 0.88 Gt Q_1 0.16 Gt 0.16 Gt P_1 0.32 Gt 0.32 Gt M_2 15.91 Gt 15.91 Gt S_2 2.65 Gt 2.65 Gt N_2 3.18 Gt 3.18 Gt K_2 0.80 Gt 0.80 Gt

Table 4.2: Baseline Simulation Parameters

being 45 Gt. This corresponds to about 10 m of maximum unmodeled sea level over the entire main body of the fjord (approximately 5000 km^2). Then, the total mass is separated into the different polynomial and periodic terms. Typical relative amplitudes of the tidal constituents are roughly respected, reflecting their natural importance. Finally, a region is defined around the mass anomaly outside which observations are discarded in the estimation process, see Figure 4.2. The size of the boundaries are chosen arbitrarily initially, but validated later in Subsection 4.2.3.

Results of the simulation in form of the estimated mass parameters is presented in Table 4.3. The first two columns show the solutions using the analytically computed

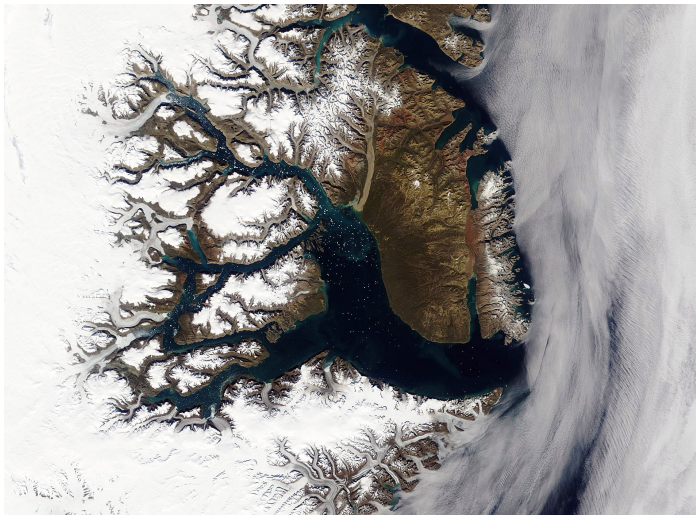

Figure 4.1: Scoresby Sound Satellite Image [22]

observable, and the last two columns use the filtering method (usually the CRN filter) to generate the range acceleration measurement. As the model does not include a constant bias in the total mass, one case each assumes knowledge of this (*No Constant*), while the other one does not (*Full*). The Mass RMSE values of each of the four solutions is included in the last row. Table 4.4 shows additional solution performance characteristics. The condition number of the mapping matrix H is in an acceptable range for the solution to be numerically stable. Furthermore, as discussed in Subsection 3.3.1, the poor performance of the numerical differentiation because of the low-quality orbit integration is reflected in the Observable and Filter RMSE.

The first thing to notice is the significant decrease of accuracy when using the default CRN-class digital filter instead of the analytic equation to differentiate the range measurement. An RMSE of 100 Mt corresponds—over the main surface of the fjord—to about 2 cm of water height, whereas 0.01 kt would correspond to about 1 nm. The larger issue is that the error in the solutions with filtered observables is not homogeneous throughout the components, but focuses on the constant bias, K_1 and

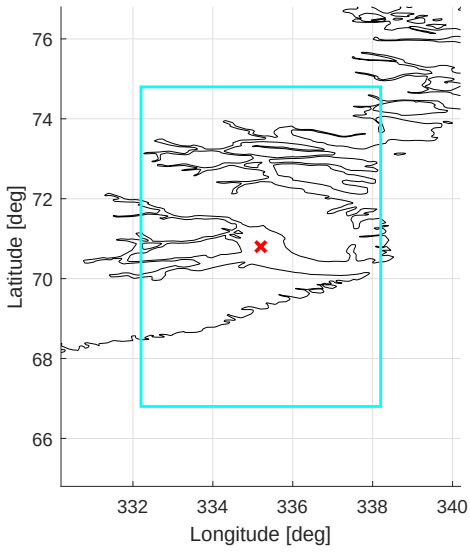

Figure 4.2: Baseline Simulation Region

K_2. As will be shown in Subsection 4.2.3, this is not exclusively due to the aliasing between K_1 and K_2, as it does occur even when no semi-diurnal frequencies are present. In fact, as Figure 4.3 shows for the filtered observables, full estimation case (blue line), the inaccurate diurnal and semidiurnal constituents are a numerical way to "match" the observed mass during flyovers, given their large error in the constant bias. The result is a significantly degraded estimated mass time series between the times when measurements are available. It therefore emphasizes the poor observability of the harmonic constituents and vulnerability to low-quality acceleration observations.

Giving the least squares problem knowledge about the nonexistence of a constant bias (i.e., not estimating it but setting it to zero) greatly reduces this problem, as Figure 4.4 shows. While the filtered observables, no constant estimated case (cyan line) is still orders of magnitude larger than the cases using analytic observables, it does follow the general trend, and just over- or underestimates peaks (see Figure 4.3, where the cyan line is mostly behind the red and black lines). Through the course of the following sensitivity analysis, this behavior of the estimated time series for both

		Analytic		Filtered	
	Model	No Constant	Full	No Constant	Full
Constant	0 t	0 t	164.75 t	0 t	-14.28 Gt
Linear	225 Mt/y	225.00 Mt/y	225.00 Mt/y	225.84 Mt/y	225.87 Mt/y
K_1^s	0.94	0.94	0.94	1.47	-3.13
K_1^c	0.94	0.94	0.94	1.03	0.12
O_1^s	0.88	0.88	0.88	0.83	0.83
O_1^c	0.88	0.88	0.88	0.86	0.86
Q_1^s	0.16	0.16	0.16	0.18	0.18
Q_1^c	0.16	0.16	0.16	0.14	0.14
P_1^s	0.32	0.32	0.32	0.31	0.31
P_1^c	0.32	0.32	0.32	0.32	0.32
M_2^s	15.91	15.91	15.91	15.91	15.91
M_2^c	15.91	15.91	15.91	15.90	15.90
S_2^s	2.65	2.65	2.65	2.61	2.61
S_2^c	2.65	2.65	2.65	2.64	2.64
N_2^s	3.18	3.18	3.18	3.23	3.23
N_2^c	3.18	3.18	3.18	3.15	3.15
K_2^s	0.80	0.80	0.80	0.49	-4.89
K_2^c	0.80	0.80	0.80	0.64	13.68
RMSE		0.01 kt	0.01 kt	109.00 Mt	113.02 Mt

Table 4.3: Baseline Simulation Results. Note the different scales for mass units. Units are Gt except where noted.

cases (with or without bias estimation) does not change. Furthermore, it should be noted that in reality, one would rarely *not* want to estimate a constant bias. For these two reasons, plots and tables for the "No Constant" cases are omitted.

For completeness, the formal standard deviation of the baseline solution is shown in Table 4.5. As suspected by the differences between the estimated and model mass parameters, the constant bias, K_1 and K_2 exhibit the largest formal uncertainties. Because of the aliasing between the components, their correlation coefficients (see Table 4.6) are high. Therefore, any slight error in one component can have a disproportionate impact on any correlated element.

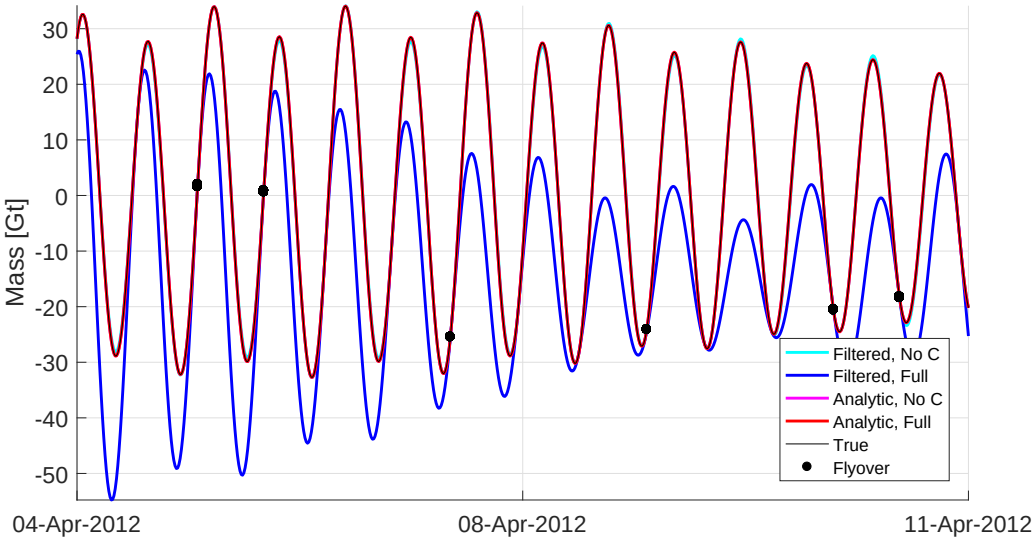

Figure 4.3: Baseline Simulation Mass Time Series (sample week)

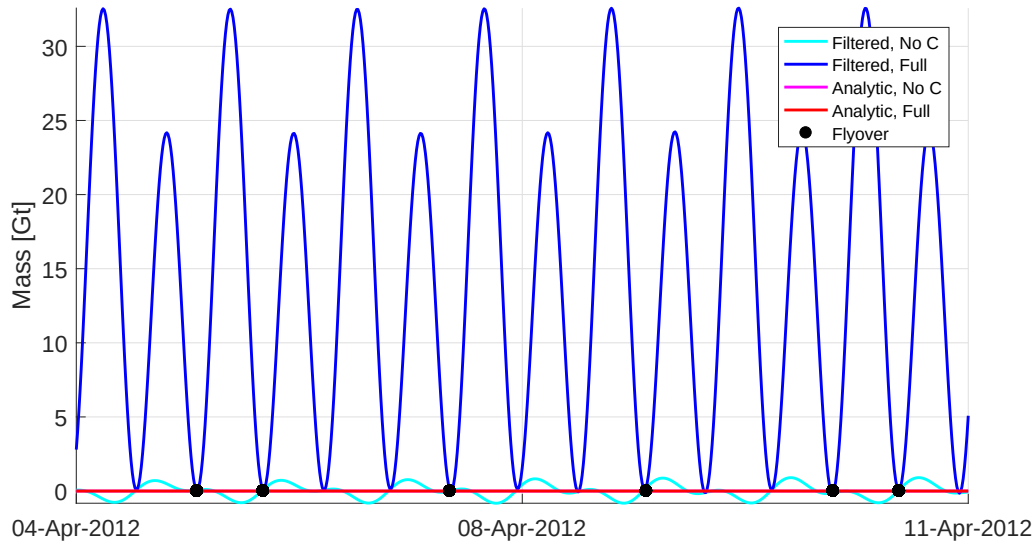

Figure 4.4: Baseline Simulation Mass Error (sample week)

Condition Number	$5.9 \cdot 10^3$
Observable RMSE	0.42 nm/s^2
Filter RMSE	0.38 nm/s^2

Table 4.4: Baseline Simulation Performance

Constant	$3.25 \cdot 10^{11}$ kg/(nm/s^2)
Linear	$1.62 \cdot 10^{8}$ kg/(y nm/s^2)

K_1^s	$1.06 \cdot 10^{11}$ kg/(nm/s^2)	M_2^s	$6.63 \cdot 10^{8}$ kg/(nm/s^2)
K_1^c	$2.11 \cdot 10^{10}$ kg/(nm/s^2)	M_2^c	$6.65 \cdot 10^{8}$ kg/(nm/s^2)
O_1^s	$6.63 \cdot 10^{8}$ kg/(nm/s^2)	S_2^s	$6.64 \cdot 10^{8}$ kg/(nm/s^2)
O_1^c	$6.64 \cdot 10^{8}$ kg/(nm/s^2)	S_2^c	$6.64 \cdot 10^{8}$ kg/(nm/s^2)
Q_1^s	$6.64 \cdot 10^{8}$ kg/(nm/s^2)	N_2^s	$6.64 \cdot 10^{8}$ kg/(nm/s^2)
Q_1^c	$6.64 \cdot 10^{8}$ kg/(nm/s^2)	N_2^c	$6.64 \cdot 10^{8}$ kg/(nm/s^2)
P_1^s	$6.64 \cdot 10^{8}$ kg/(nm/s^2)	K_2^s	$1.23 \cdot 10^{11}$ kg/(nm/s^2)
P_1^c	$6.64 \cdot 10^{8}$ kg/(nm/s^2)	K_2^c	$2.97 \cdot 10^{11}$ kg/(nm/s^2)

Table 4.5: Baseline Simulation Formal Standard Deviation

4.2.3 Sensitivity Analysis

After presenting the baseline simulation, the influence of the multitude of different parameters in the simulation and computation steps needs to be assessed. They can roughly be separated into settings of the filter (e.g. type, window, bandwidth), of the mass anomalies (e.g. number, geometry, mass variability), as well as of the simulation itself (e.g. time span, regional restriction), and are going to be ordered in that fashion. Three purposes are being served: First, a set of parameters can be determined that enable the (relatively) best solution given simulated orbit data. Second, if certain criteria have a significantly larger impact on the results than others, this should be noted for future work using real GRACE data. Third, it is verified if the significant inconsistencies of the CRN filter with simulated data are also due to simulation parameters and can be mitigated.

	C	Lin	K_1^s	K_1^c	O_1^s	O_1^c	Q_1^s	Q_1^c	P_1^s	P_1^c	M_2^s	M_2^c	S_2^s	S_2^c	N_2^s	N_2^c	K_2^s	K_2^c
C	1	0	1	1	0	0	0	0	0	0	0	0	0	0	0	0	1	-1
Lin	0	1	0	0	0	0	0	0	0	0	0	0	0	0	0	0	0	0
K_1^s	1	0	1	1	0	0	0	0	0	0	0	0	0	0	0	0	1	-1
K_1^c	1	0	1	1	0	0	0	0	0	0	0	0	0	0	0	0	1	-1
O_1^s	0	0	0	0	1	0	0	0	0	0	0	-0.1	0	0	0	0	0	0
O_1^c	0	0	0	0	0	1	0	0	0	0	0.1	0	0	0	0	0	0	0
Q_1^s	0	0	0	0	0	0	1	0	0	0	0	0	0	0	0	-0.1	0	0
Q_1^c	0	0	0	0	0	0	0	1	0	0	0	0	0	0	0.1	0	0	0
P_1^s	0	0	0	0	0	0	0	0	1	0	0	0	0	-0.1	0	0	0	0
P_1^c	0	0	0	0	0	0	0	0	0	1	0	0	0.1	0	0	0	0	0
M_2^s	0	0	0	0	0	0.1	0	0	0	0	1	0	0	0	0	0	0	0
M_2^c	0	0	0	0	-0.1	0	0	0	0	0	0	1	0	0	0	0	0	0
S_2^s	0	0	0	0	0	0	0	0	0	0.1	0	0	1	0	0	0	0	0
S_2^c	0	0	0	0	0	0	0	0	-0.1	0	0	0	0	1	0	0	0	0
N_2^c	0	0	0	0	0	0	0	0.1	0	0	0	0	0	0	1	0	0	0
N_2^c	0	0	0	0	0	0	-0.1	0	0	0	0	0	0	0	0	1	0	0
K_2^c	1	0	1	1	0	0	0	0	0	0	0	0	0	0	0	0	1	-1
K_2^c	-1	0	-1	-1	0	0	0	0	0	0	0	0	0	0	0	0	-1	1

Table 4.6: Baseline Simulation Correlation Matrix

Impact of Different CRN Filter Parameters

Test cases with $N_c = 3, 5, 7, 9$, $T_f \approx 70\,\text{s}, 100\,\text{s}$ and $B_t = 0.05\,\text{Hz}, 0.10\,\text{Hz}$ and their respective performance indices are shown in Table 4.7. Figure 4.5 shows that the halving of the bandwidth has a large impact on the RMSEs of the filter and the observable. Additionally, while the filter time span has a small impact on the performance when using $B_t = 0.10$ Hz, it becomes a factor when reducing the bandwidth. However, as Figure 4.6 suggests, these improvements are not large enough to overcome the errors between flyovers presented in Subsection 3.3.1, as the resulting Mass RMSEs are still multiple orders of magnitude above the ones created using analytic observables.

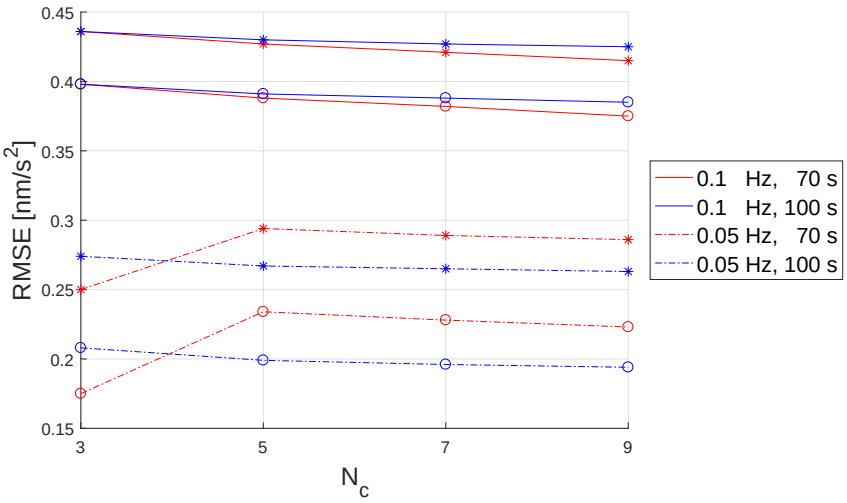

Figure 4.5: Impact of Number of Convolutions, Filter Window Length and Bandwidth on the Filter RMSE. *Circles:* Filter, *Stars:* Observable

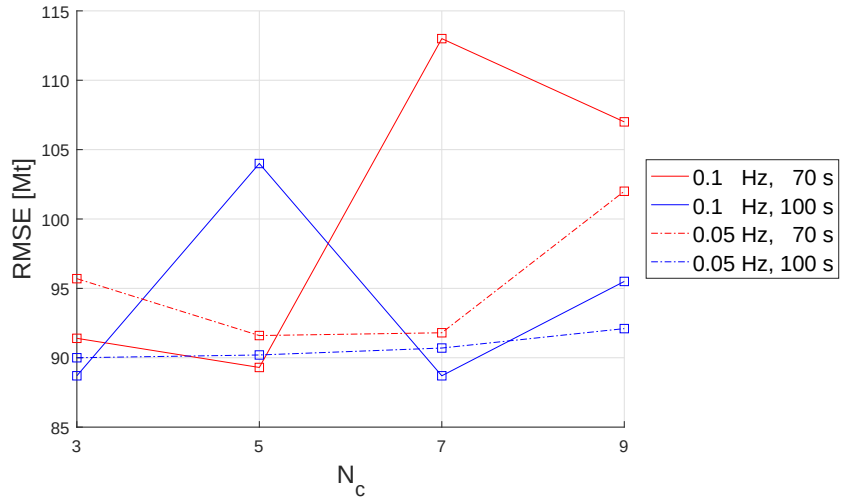

Figure 4.6: Impact of Number of Convolutions, Filter Window Length and Bandwidth on the Filtered Mass RMSE

N_c	T_f [s]	B_t [Hz]	RMSE Mass [Mt]	RMSE Filter [nm/s^2]	RMSE Observable [nm/s^2]
3	69.9	0.05	95.70	0.17	0.25
		0.10	91.35	0.40	0.44
	99.9	0.05	90.02	0.21	0.27
		0.10	88.68	0.40	0.44
5	70.5	0.05	91.56	0.23	0.29
		0.10	89.29	0.39	0.43
	100.5	0.05	90.18	0.20	0.27
		0.10	104.44	0.39	0.43
7	70.7	0.05	91.79	0.23	0.29
		0.10	113.02	0.38	0.42
	100.1	0.05	90.73	0.20	0.27
		0.10	88.74	0.39	0.43
9	71.1	0.05	101.83	0.22	0.29
		0.10	107.09	0.37	0.42
	99.9	0.05	92.10	0.19	0.27
		0.10	95.48	0.39	0.42

Table 4.7: Impact of Number of Convolutions, Filter Window Length and Bandwidth. The baseline case is highlighted. The Analytic Mass RMSEs are identical to the baseline case.

Use of Polynomial Filter

To validate the implemented code and have an alternative differentiating filter to the CRN method, a polynomial filter is designed to compare the observables and the inferred mass. A 5th-order polynomial is fit through the measurements at every time step using the same filter window length T_f as before. The derived function is then differentiated to generate range rate and acceleration, and evaluated at the center point.

Table 4.8 shows the performance of the filter in terms of the RMSEs. While the Filter and Observable errors are significantly reduced, the Mass RMSE is actually increased. This is most likely due to the inherent limitations of approximating extrema of sinusoidal time series using a low-order polynomial.

	RMSE		
Filter	Mass [Mt]	Filter [nm/s^2]	Observable [nm/s^2]
CRN	113.02	0.38	0.42
Polynomial	182.44	0.07	0.19

Table 4.8: Impact of Polynomial Filter. The baseline case is highlighted. The Analytic Mass RMSEs are identical to the baseline case.

No Linear or Semidiurnal Components

As Table 4.9 and Table 4.10 show, the poor performance of the estimation using filtered observables can not be tied exclusively to the Constant, K_1 and K_2 triple, as Table 4.3 might have suggested. The absolute values of the estimated constituents still digress non-uniformly from the model, showing large differences in the periodic and constant components. Furthermore, the condition number is still high, and the Observable and Filter RMSEs do not reduce.

The cases using analytical measurements perform as well as before.

Two Mascons

A second mascon is added to the simulation, and test cases are run where the two mascons are separated by $\Delta\text{Lon} = 0$ deg, but $\Delta\text{Lat} = 0.5, 1, 5, 15$ deg. The mass variations structure is the same as the baseline case for each mass anomaly, except that the total mass is conserved by dividing it in two, thus resulting in smaller individual amplitudes. Figure 4.7 shows that while, relatively, a separation of only 1 deg or less is much worse than a larger separation, it is still possible to estimate the anomalies in both grids. This gives confidence in the previously chosen 3-by-4 degree grid sizes. (The boundaries to restrict measurements are now applied to each of the mascons.)

Component	No Linear Model	No Linear Analytic	No Linear Filtered	No Semidiurnal Model	No Semidiurnal Analytic	No Semidiurnal Filtered
Constant	0 t	475.35 t	61.41 Mt	0 t	2.76 t	-77.90 Mt
Linear				225 Mt/y	225.00 Mt/y	247.58 Mt/y
K_1^s	0.94	0.94	1.40	0.94	0.94	1.66
K_1^c	0.94	0.94	1.00	0.94	0.94	1.07
O_1^s	0.88	0.88	0.90	0.88	0.88	0.91
O_1^c	0.88	0.88	0.93	0.88	0.88	0.91
Q_1^s	0.16	0.16	0.12	0.16	0.16	0.10
Q_1^c	0.16	0.16	0.09	0.16	0.16	0.14
P_1^s	0.32	0.32	0.36	0.32	0.32	0.38
P_1^c	0.32	0.32	0.28	0.32	0.32	0.30
M_2^s	15.91	15.91	15.95			
M_2^c	15.91	15.91	15.89			
S_2^s	2.65	2.65	2.65			
S_2^c	2.65	2.65	2.57			
N_2^s	3.18	3.18	3.20			
N_2^c	3.18	3.18	3.20			
K_2^s	0.80	0.80	0.80			
K_2^c	0.80	0.80	0.72			
RMSE Mass		0.01 kt	114.76 Mt		0.00 kt	103.3 Mt

Table 4.9: Impact of Mass Variability Structure. Note the different scales for mass units. Units are Gt except where noted.

Size of Regional Restriction

Table 4.11 shows that the region to restrict the measurements around the mass anomaly is only a minor factor for the performance of the overall solution when using filtered observation, thus not having an impact on the performance of the CRN filter (which would decrease the difference between the Filter and Observable RMSE). While a larger region slightly decreases the Mass RMSE for the analytic observable, all region size choices remain in approximately the same order of magnitude. Therefore, the choice of the region size when examining a single mass anomaly is not a critical design choice.

	No Linear	No Semidiurnal
Condition Number	$1.4 \cdot 10^3$	$0.2 \cdot 10^3$
Observable RMSE	0.41 nm/s^2	0.41 nm/s^2
Filter RMSE	0.37 nm/s^2	0.37 nm/s^2

Table 4.10: Impact of Mass Variability Structure

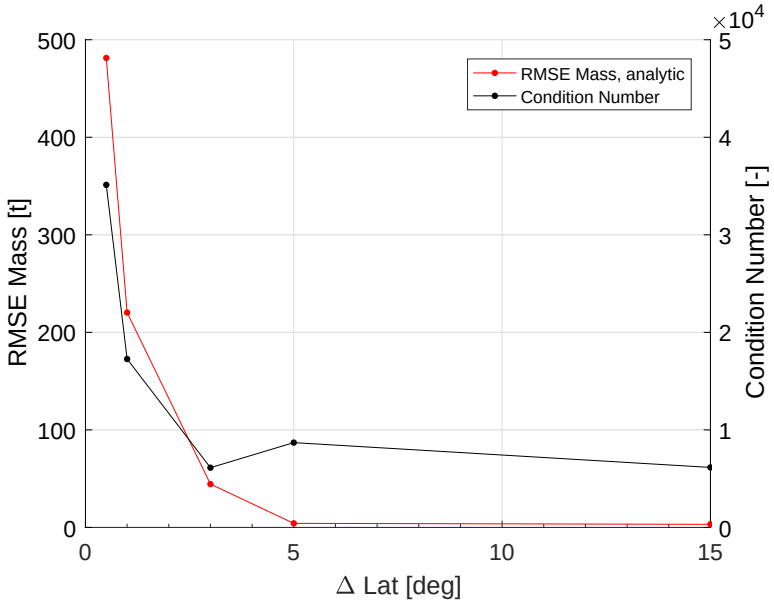

Figure 4.7: Impact of Adding a Second Mascon

Global vs. Regionally Restricted Measurements

Increasing the available measurements to encompass all time steps, and therefore the whole orbit around the globe, yields a notable improvement in the condition number of the problem, see Table 4.12. This results in most correlation coefficients that used to be close to 1 (compare Table 4.6) to drop to about 0.3 to 0.8; only the Constant-K_2 remains 1. The Mass RMSE, using the analytic observable to estimate the solution, can also be slightly reduced.

An important caveat to note here is that only one mass anomaly was included, so the validity of this result when expecting multiple mass anomalies to be present in

ΔLon [deg]	ΔLat [deg]	RMSE Mass, A. [t]	Mass, F. [Mt]	Filter [nm/s^2]	Obs. [nm/s^2]
1	2	25.21	123.77	0.36	0.40
3	4	8.65	113.02	0.38	0.42
5	6	6.11	92.87	0.38	0.41

Table 4.11: Impact of Size of Region. The baseline case is highlighted. Note the different scales for mass units.

the simulation is not guaranteed.

	Condition Number		Analytic Mass RMSE	
	5 years	10 years	5 years	10 years
Regional	3157.2	8689.6	8.7 t	8.7 t
Global	44.8	84.3	1.7 t	2.5 t

Table 4.12: Influence of Regionally Restricting Measurements

Simulation Time Span

Restricting available measurements to a small grid element greatly reduces the information content available to the least squares problem, which can theoretically be countered by increasing the time span during which data is collected. Figure 4.8 shows the RMSEs of the mass time series and the filter output for time spans between 1 and 10 years (note the different scaling factors). The Mass RMSE of the analytic observable stays approximately constant and shows no trend between the different time spans, indicating that given accurate observations, reliable estimates can be computed using only a couple of year's data.

For completeness, the results using the low-quality filtered observable are shown as well, being consistently poor, but constantly improving with more data. This is most likely due to effect of averaging out the higher-frequency noised introduced by the CRN filter. However, this trend is not likely to continue forever, as the

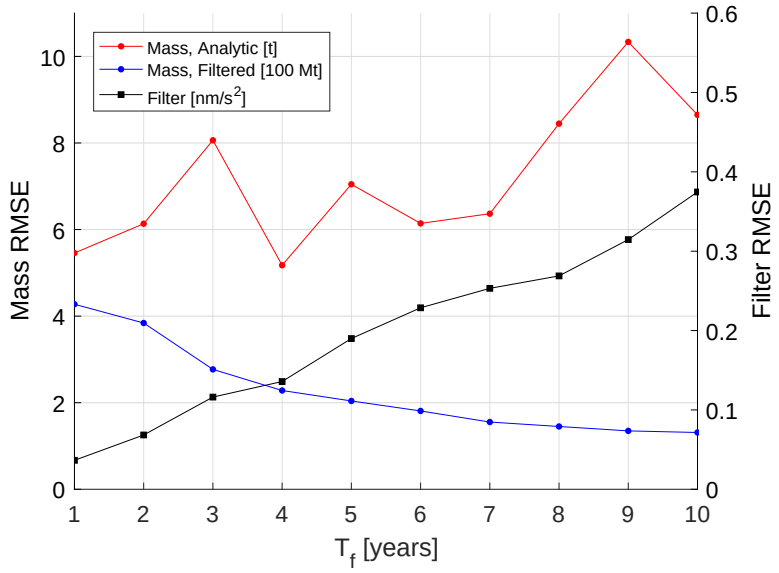

Figure 4.8: Impact of Simulation Time Span

filter error increases steadily (also compare Figure 3.5).

Sampling Frequency and Measurement Noise

Table 4.13 shows simulations run to test whether the estimate improves when increasing the sampling frequency from the current GRACE default of 0.2 Hz up to the native measurement frequency of 10 Hz. Interestingly, an increase in available data does increase the Mass RMSEs slightly (for a total time span of 10 years of simulation, and no added measurement noise). For the estimate using the analytic observable, this is possibly due to accumulation of errors in the mapping matrix, which is computed using the nominal (not true) orbit. For the estimate with the filtered observable, it might have a reduced effect given the poor quality of the differentiated observable. In general, though, this supports the current standard of using 0.2 Hz data, which has the additional benefit of reduced computation time.

When adding measurement noise (white, $\sigma_{\text{obs}} = 2\,\text{nm/s}^2$) to both the analytic

f_s [Hz]	Mass RMSE, no noise Analytic	Filtered	Mass RMSE, with noise Analytic	Filtered
0.2	$8.38 \cdot 10^{-6}$	129.71	573.92	390.67
1	$8.54 \cdot 10^{-6}$	131.25	194.87	273.04
10	$8.65 \cdot 10^{-6}$	131.19	43.28	165.48

Table 4.13: Impact of Sampling Frequency. The baseline case is highlighted. Units are Mt except where noted.

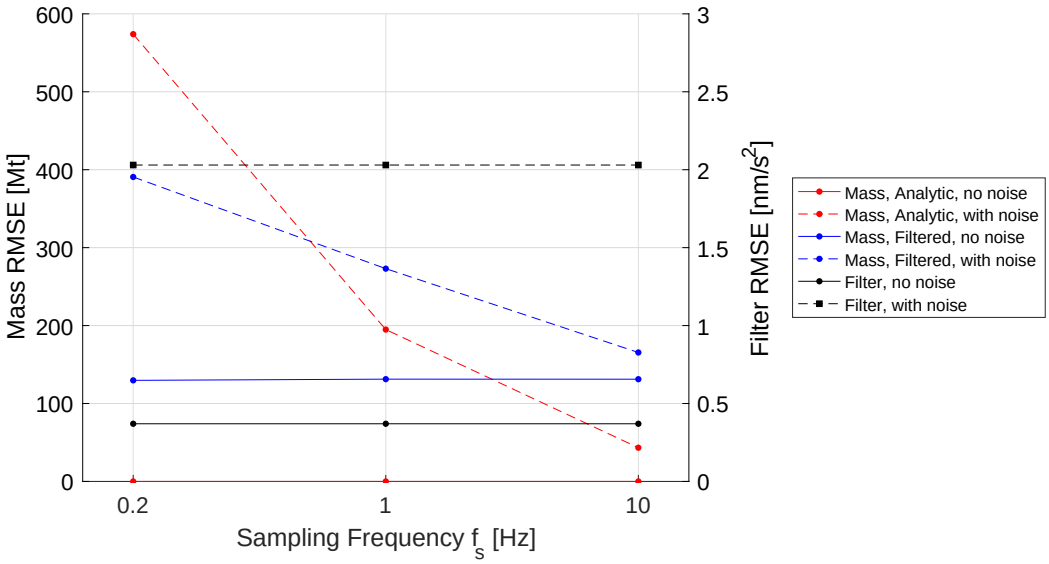

Figure 4.9: Impact of Sampling Frequency

and filtered observable (again for a time span of 10 years), three key results change, see Figure 4.9. First, the analytic observable produces mass time series estimates on the same order of magnitude than the filtered observables. Second, for the 5 s sampling rate, the analytic Mass RMSE is actually *higher* than the filtered Mass RMSE—indicating the noise reducing effect of the CRN filter. Third, an increased sampling frequency does significantly change the Mass RMSE by up to one order of magnitude.

The Filter RMSE now also mirrors the imposed noise variance σ_{obs}.

Summary

Given the results of the sensitivity analysis, the three goals that motivated this sensitivity analysis are reproduced and addressed in the following.

- **Set of "best" simulation parameters.** As the sensitivity analysis showed, most changes had either a negligible (CRN parameters, increasing grid size, different polynomial and periodic constituents, total time span, sampling frequency) or a negative (decreasing grid size, using a different filter altogether) effect on the estimation problem. This supports the current best practices. The only parameter that somewhat affected the result was the decrease of the CRN filter bandwidth when using analytic observables.

- **Identification of large-impact parameters.** The largest influence by far was between using the analytic (true) and filtered observable, given the latter's already mentioned differentiation issues. Addressing these issues will be paramount when going forward. The second key takeaway is that when using observation corrupted by white noise, increasing the sampling frequency can improve mass time series estimates significantly.

- **Verification of CRN filter issues.** Unfortunately, no changes made to the simulation setup (number of filter convolutions, low-pass bandwidth, filter length, regional restriction, removal of polynomial or periodic constituents) could change the poor behavior of the direct double derivative version of the CRN filter for simulated data.

4.3 GRACE Acceleration Residuals Using Editing Orbits

As the simulations in Subsection 4.2.2 have shown, it is theoretically possible to estimate mass anomalies using gridded observations, given high quality range acceleration measurements. In this section, an attempt is made to find mass anomalies using GRACE data. As explained in Subsection 2.3.2, range acceleration residuals act as a proxy when identifying regions where the mass variability is not fully understood. Searching for spatial patterns in the residual accelerations is therefore a viable first step in the direction of investigating anomalous mass time series that give rise to the unmodeled acceleration residuals. In this section, GRACE range acceleration residuals as output by the orbit integration and gravity field estimation procedure are used. They are the difference (O-C) between the observed DOWR range acceleration, and the range acceleration as implied by the GRACE editing orbits.

So far, the simulations in this work that aimed to estimate mass anomalies have been carried out using 10 Hz rate measurements. However, Figure 3.13 of Subsection 3.3.2 has suggested that it is more important to have accurate range acceleration residuals, than to have more observations—if the latter rely on using interpolated orbits and applying the CRN filter twice. Therefore, the native 0.2 Hz sampling frequency of the GRACE range acceleration residuals is kept.

Figure 4.10 shows the standard deviations of the range acceleration residuals in each grid element for the time span between 2005 and 2015. Clearly, the variability is higher in some regions around the globe than others, confirming the assessment presented in the beginning of this study that processes there are not fully understood and modeled yet.

Using (2.18) on a grid-by-grid basis, a linear trend and periodic variations can be fitted to the residual accelerations accumulated over the 11 year time span. If the

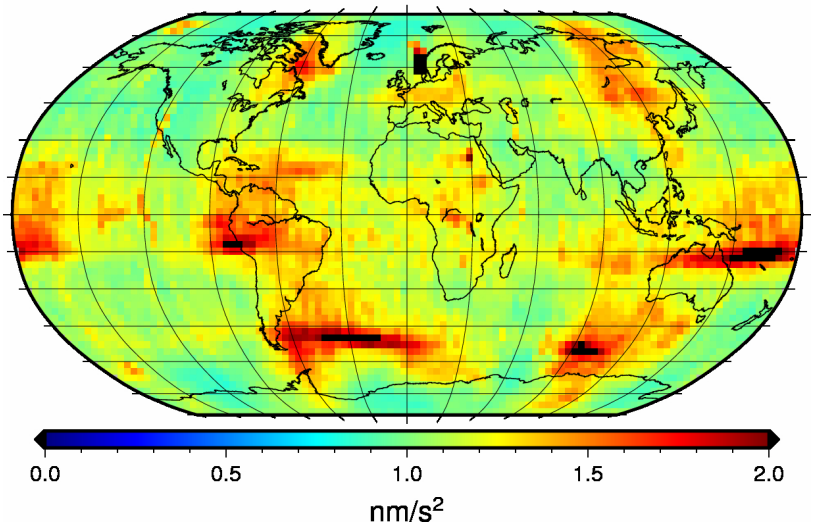

Figure 4.10: Standard Deviation of GRACE Range Acceleration Residuals for the period of 2005–2015, plotted in 3 degree bins.

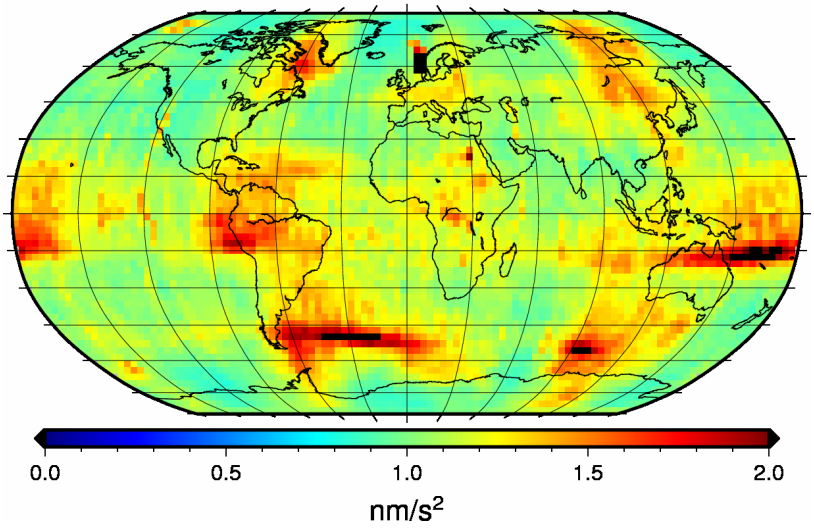

Figure 4.11: Standard Deviation of the GRACE Range Accelerations after removing the Fit for the period of 2005–2015, plotted in 3 degree bins.

variability in the grid is mostly noise, the coefficients for the polynomial and periodic basis functions would tend towards zero. If nonzero coefficients do emerge, however, we expect this bin to still contain a signal that is yet to be incorporated into the models.

As Figure 4.13 and Figure 4.14 show, most estimated grid coefficients are indeed close to zero. In regions that exhibit large total standard deviations, this indicates that the variability is either due to noise, or is not explainable by any of the polynomial terms or tidal frequencies that were assumed in the fitting model. In some areas, however, the constant bias, K_1, O_1 and M_2 components of the fit do present clear spatial patterns (e.g. O_1 between Antarctica and Australia, or M_2 around the Amazon basin). This indicates that further investigation to understand the local activity is warranted.

The total fit function is then the sum of the periodic part (as defined by the coefficient and harmonic frequencies) and the polynomial part (using the constant bias and linear trend). The variability of the periodic fit indicates which regions' acceleration residuals could best be fit by the model (Figure 4.12). After removing the total fit function for each grid from the whole time series, the new acceleration residuals variability is shown in Figure 4.11. While the standard deviations did decrease in the most prominent regions, it did not have a significant impact.

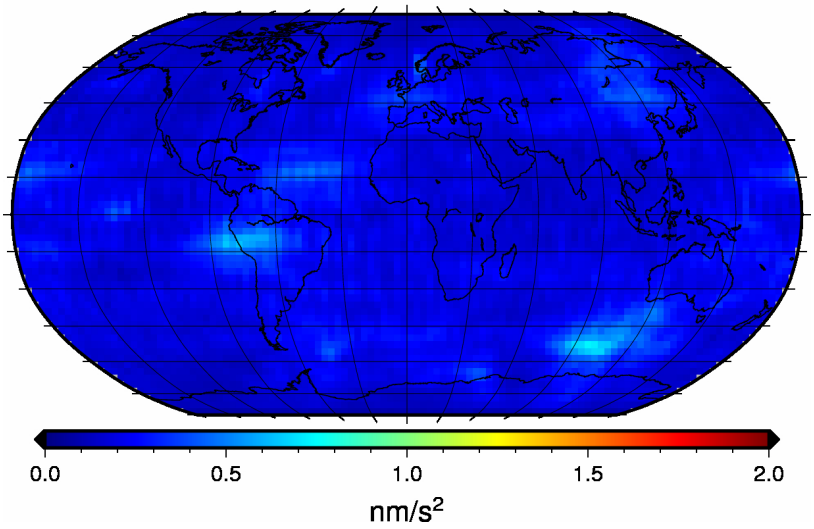

Figure 4.12: Standard Deviation of the Periodic Fit for the period of 2005–2015, plotted in 3 degree bins.

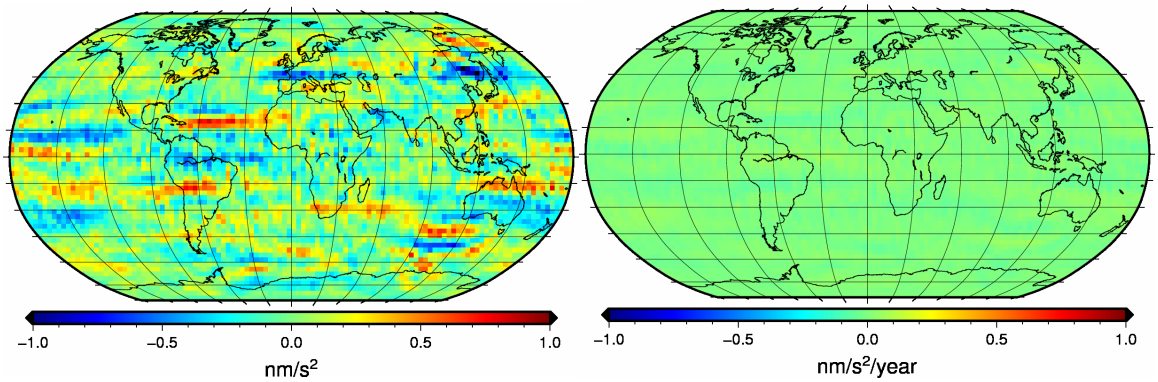

(a) Constant (b) Linear

Figure 4.13: Estimated Polynomial Fit Coefficients for GRACE Acceleration Residuals for the period of 2005-2015, plotted in 3 degree bins.

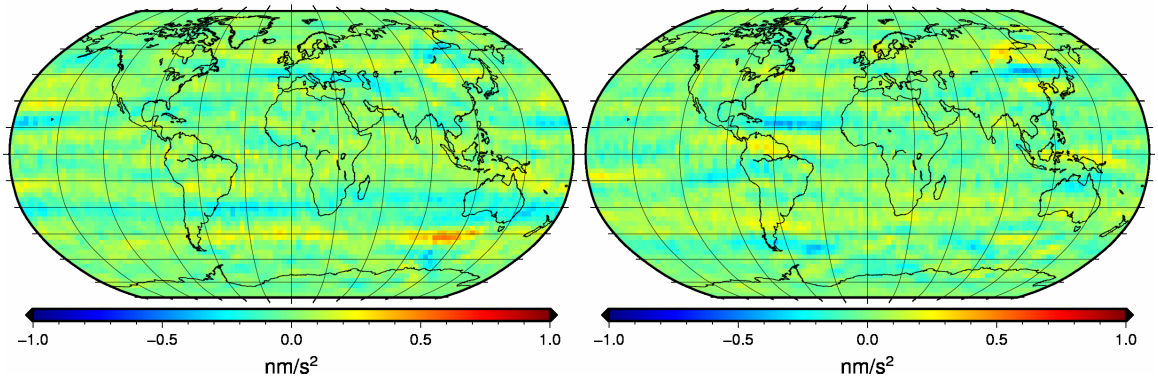

(a) K_1^s (b) K_1^c

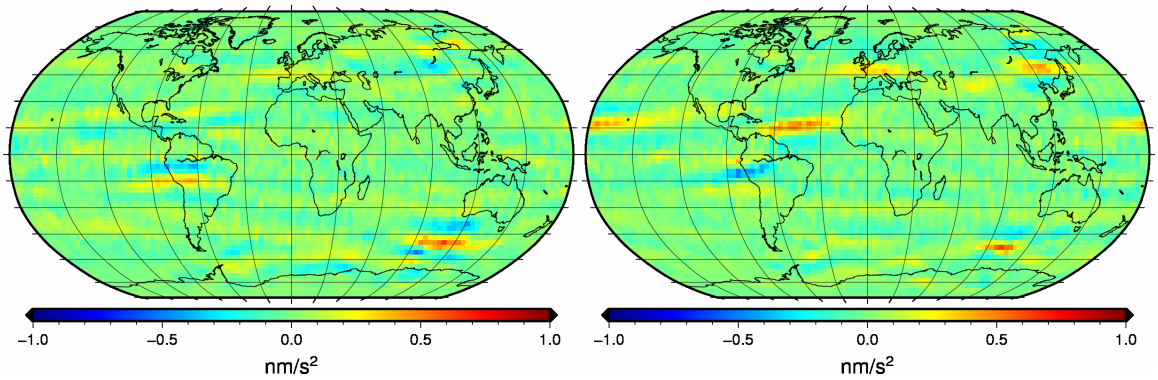

(c) O_1^s (d) O_1^c

Figure 4.14: *Continued next page*

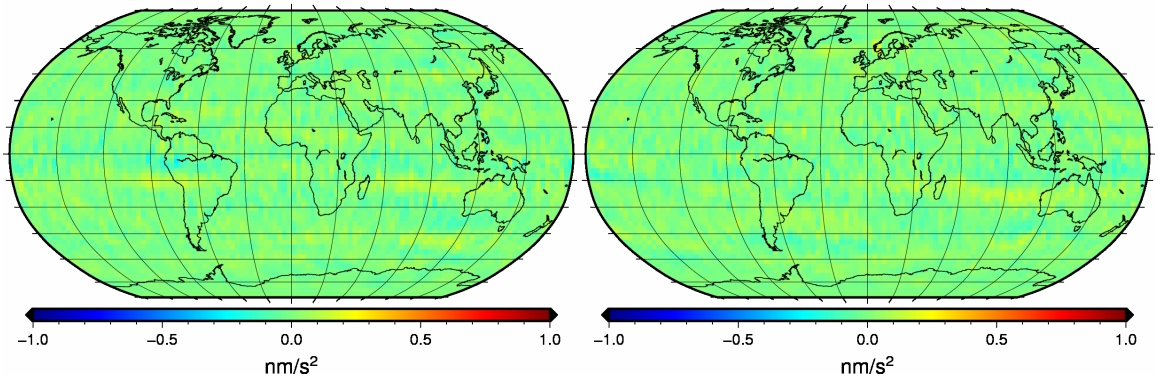

(e) Q_1^s (f) Q_1^c

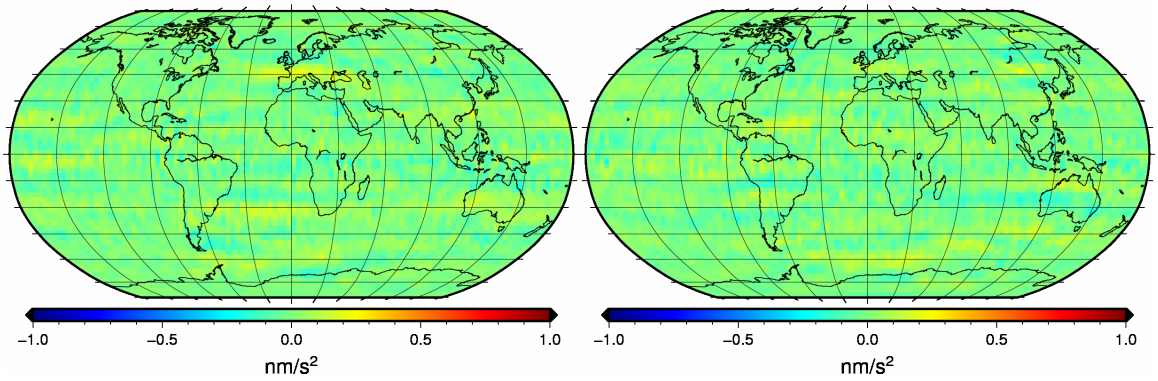

(g) P_1^s (h) P_1^c

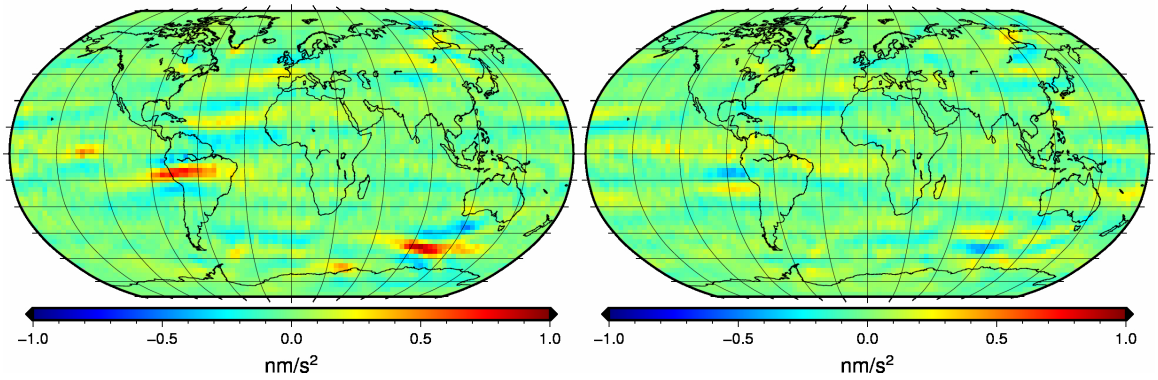

(i) M_2^s (j) M_2^c

Figure 4.14: *Continued next page*

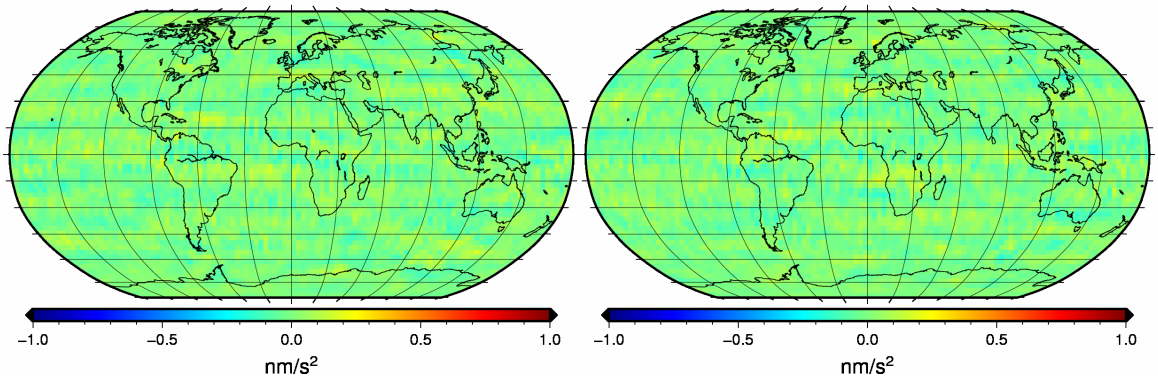

(k) S_2^s (l) S_2^c

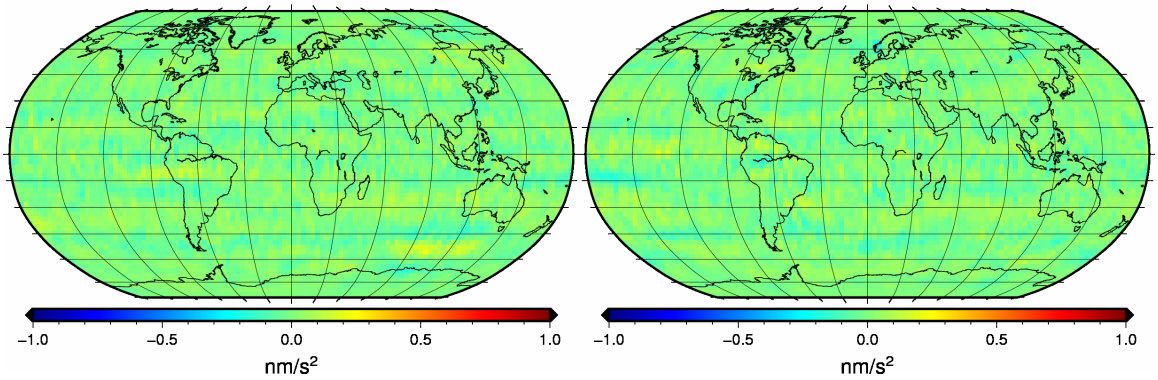

(m) N_2^s (n) N_2^c

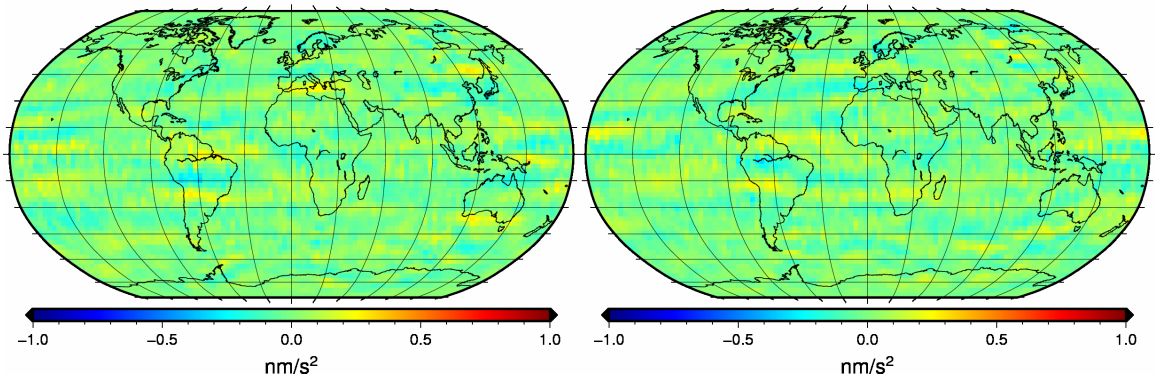

(o) K_2^s (p) K_2^c

Figure 4.14: Estimated Periodic Fit Coefficients for GRACE Acceleration Residuals for the period of 2005–2015, plotted in 3 degree bins.

Chapter 5

Conclusion

This chapter will conclude the study by presenting key findings and putting them into context. First, the main results of the simulations and data analyses are summarized in Section 5.1. Then, Section 5.2 will suggest a way forward.

5.1 Summary

The center of this work has been the development and use of a simulation and estimation framework to infer local mass anomalies using regionally restricted, GRACE-like observations. Starting from first principles, the equations of motion of a particle under the influence of other point masses (the N-body problem) were derived to lay the mathematical groundwork to simulate the satellite's orbits. Separating the terms of known influence on the satellites (simplified to be the spherical, homogeneous Earth) from each spacecraft's absolute acceleration led to a linear least squares formulation to estimate mass variations using inter-satellite range acceleration measurements.

To generate simulated acceleration measurements, two methods were introduced. First, analytical equations were derived to directly compute absolute spacecraft acceleration as a function of all the masses present in the system, including the mass anomalies (referred to as the analytic observable). This true acceleration would not be obtainable in real life applications, which is why the second approach used range (as can be output quite precisely using the onboard microwave ranging instrument) and a CRN-class digital filter to create range acceleration observations

(called filtered observables). This process, however, yielded significantly worse results when used with anything other than actual GRACE data. Specifically, it has introduced high-frequency variations in its second derivative output when used on simulated range measurements, attaining an RMSE of about 0.4 nm/s^2—only an order of magnitude below the analytical range acceleration itself. This behavior is most likely due to the the low quality orbits produced by Matlab's standard integrators.

Using ten years of simulated orbits, consisting of point-mass Earth, one mass anomaly and two satellites, measurements were then restricted to a region in close proximity to the mass anomaly. The analytic and filtered observations were each used independently to infer the anomaly's mass variability. In the former case, the estimated solution was very accurate, with the Mass RMSE being less than a kiloton for a total signal of up to several gigatons (corresponding to about a nanometer of water height over the surface area analyzed). It also proved to be robust when changing the number of mass anomalies simulated, their respective geometry, or their variability function.

Using the filtered observables, however, failed to achieve an accurate solution because of the digital filter's insufficiencies when operating on the simulated data. Inferring the mass time series yielded total Mass RMSEs of more than 100 Mt for the same truth model as above (comparable to 2 cm of water height over the surface area), and individual error components of several gigatons. A sensitivity analysis was performed to assess the influence of filtering and simulation parameters such as the size of the regional restriction, the mass variability structure, and the CRN parameters on the estimation results. All changes, however, were negligible compared to the loss of quality in going from analytical to filtered observables.

As inter-satellite range acceleration is proportional to the masses exerting in-

fluence on the spacecraft, spatial patterns in the former will also be present in the latter. Using GRACE mission data from 2005 to 2015 and dividing the data into grid elements spanning Earth's surface, regions of higher acceleration residuals variability were identified. Specifically, regions around the Falkland Islands, in the South Indian Ocean, in Northeastern Australia, and around Peru exhibited a range acceleration standard deviation of up to 2 nm/s^2.

Finally, polynomial and periodic coefficients were fit to the acceleration residual time series of each grid element to assess whether the variability could be explained by noise, or if there was actually a signal to be investigated. The estimation process yielded fitting functions, whose largest components (for the same regions mentioned above) were the constant bias, K_1, O_1, M_2 and K_2, reaching up to ± 1 nm/s^2 in amplitude. However, the overall reduction in the variability of the residuals was not particularly significant.

5.2 Outlook

As the significant difference in the mass estimation results between the analytical and filtered observable show, data quality is the single largest influence on whether local signals can be resolved. Several observations can be made:

- Given accurate measurements and a detailed background force model, restricting the measurements spatially does allow for local mass anomalies to be estimated.

- Special attention should be given to the quality of the orbit propagator and to the numerical differentiation methods to avoid the introduction of noise when generating acceleration observables.

- When trying to reduce the variability in the GRACE mission's range acceleration residuals, fitting functions may need to be more sophisticated than the ones used in this study to entail a significant improvement.

The full potential of currently available observations, therefore, still needs to be reached. Going forward, similar simulation studies using higher quality orbit integrators (such as MSODP) should be conducted to validate the preliminary results presented here. Furthermore, a deeper investigation of the numerical processes giving rise to the issues of the CRN filter when used in its second-order version could yield improvements to the filter (possibly in the form of higher-precision computing), or consensus on when to avoid using it. These assessments will be essential in the future, as the quality of the measurements increases with upcoming missions like GRACE Follow-On, and data analysis methods could be the limiting factor in the solution quality.

Appendix A

Algorithms

A.1 Hermite Interpolation

(This appendix uses different indices and ranges than the rest of this work for readability purposes.)

GRACE position and velocity data is computed and stored for 5 s intervals. When the satellite's state is needed at intermediate times for post-processing applications, Hermite interpolation can be applied. It is based on the Lagrange interpolation function, which fits a polynomial of degree $n-1$ *exactly* through n data tuples (t_k, x_k), called knots. Hermite interpolation additionally requires that the polynomial's derivative pass through the derivatives of the knots at $(t_k, \dot{x}_k)$ [23, Ch. 1]. This is particularly useful, as orbit solution for GRACE are precisely known in position and velocity, and thus the velocity information can be used to smoothen the position time series. By adding the derivative constraints, the degree of the interpolator increases to $2n-1$. The Hermite interpolating function is then given by

$$\begin{aligned} f(t) &= \sum_{k=1}^{n} U_k(t) x_k + \sum_{k=1}^{n} V_k(t) \dot{x}_k \\ \dot{f}(t) &= \sum_{k=1}^{n} \dot{U}_k(t) x_k + \sum_{k=1}^{n} \dot{V}_k(t) \dot{x}_k \end{aligned} \tag{A.1}$$

for each coordinate x, y, z. In order to match the knot values x_k and their derivatives

$\dot{x}_k$ at the knot times t_k, the auxiliary functions $U_k(t)$ and $V_k(t)$ suffice

$$U_k(t_j) = \delta_{jk} \qquad V_k(t_j) = 0$$
$$\dot{U}_k(t_j) = 0 \qquad \dot{V}_k(t_j) = \delta_{jk}$$

where δ_{jk} is the Kronecker delta. This is enabled by choosing

$$U_k(t) = \Big(1 - 2(t - t_k)\dot{L}_k(t_k)\Big) L_k^2(t)$$
$$V_k(t) = (t - t_k)L_k^2(t)$$

Their derivatives are therefore

$$\dot{U}_k(t) = 2\left(\dot{L}_k(t) - \dot{L}_k(t_k)L_k(t) - 2(t - t_k)\dot{L}_k(t_k)\dot{L}_k(t)\right) L_k(t)$$
$$\dot{V}_k(t) = L_k^2(t) + 2(t - t_k)L_k(t)\dot{L}_k(t)$$

$U_k(t)$ and $V_k(t)$ are defined using the Langrange interpolating polynomial

$$L_j(t) = C_j \prod_{\substack{k=1 \\ k\neq j}}^{n} (t - t_k) \qquad \text{where} \quad C_j = \prod_{\substack{k=1 \\ k\neq j}}^{n} (t_j - t_k)^{-1} \tag{A.2}$$

and its derivative

$$\dot{L}_j(t) = C_j \sum_{\substack{k=1 \\ k\neq j}}^{n} \prod_{\substack{l=1 \\ l\neq j,k}}^{n} (t - t_l)$$

sufficing $L_j(t_i) = \delta_{ij}$ to match the knot values.

While Hermite interpolating functions are smooth in x, and continuous in $\dot{x}$, no guarantee can be made about the smoothness of $\dot{x}$. In fact $\dot{f}(t)$ usually exhibits oscillatory behavior between the knot times t_k, especially when approximating sinusoidal functions. This effect is mitigated by keeping the number of knots low ($n = 4$

for GRACE), effectively reducing the order of the polynomial. This implies that the interpolator is now defined piecewise, i.e. only the four closest knots to the target time are used to interpolate the data series. A piecewise Hermite interpolator, however, will exhibit discontinuities in the derivatives at the knot tuples, another important negative side effect, that needs to be considered when using a digital filter on the interpolated data.

A.2 Time Systems

It should be noted that given the different data inputs, different time systems have to be used. Specifically,

- GRACE satellite clocks (GRC) are synchronized with the GPS time system to date measurements. As such, they don't observe leap seconds. However, they are not counted in weeks and seconds since the GPS epoch is at midnight January 6, 1980, but use (only) seconds since noon, January 1, 2000 (referenced as the J2000 epoch).

- Julian Date (JD) is counted as days since noon Universal Time (UT) on January 1, 4713 BC. It is tied to Earth's position relative to the sun, and most commonly used in its Universal Time Coordinated (UTC) variant (the difference between UT and UTC being kept at less than 0.9 s at every point in time by the introduction of leap seconds).

- Tide calculations rely on ephemerides of Earth, Moon and the Sun. Since 2001, the time system used for astronomical observations is Terrestrial Time (TT), a theoretical time system approximated post-factum.

- The Greenwich Apparent Sidereal Time (GAST) can be understood as the local solar time at every point on Earth, meaning that noon will always coincide with the highest sun elevation angle. GAST can be derived from JD.
- To convert between the Earth-Centered Inertial and Earth-Fixed frames, the rotation angle of Earth with respect to the J2000 epoch is needed. It is calculated using hour angles, derived from GAST.

GPS is always 19 seconds behind of TAI, and TAI is always 32.184 seconds behind TT [24, Recommendation IV], therefore

$$\mathrm{TT} = \mathrm{TAI} + 32.184\ \mathrm{s} = \mathrm{GPS} + 32.184\ \mathrm{s} + 19\ \mathrm{s}$$

The conversion between GRACE seconds to JD follows

$$\mathrm{JD} = (\mathrm{GRC} - \mathrm{LS})/86400\ {}^{\mathrm{s}}/_{\mathrm{d}} + 2451545\ \mathrm{d}$$

and satisfies the different epochs of GRC and GPS. LS denotes the leap seconds introduced to UTC since the start of GPS time.
Finally, GAST can be computed as described by the US Naval Observatory [25].

A.3 Reference Frames

For simplicity, converting between the Earth-Centered, Earth-Fixed (ECEF) and Inertial (ECI) reference frame is reduced to a single rotation about the Earth's z-axis. The rotation angle between the ECI reference x-axis and the instantaneous

ECEF x-axis is given by the aforementioned hour angle:

$$\gamma = \text{GAST}/24\ \text{h} \cdot 2\pi$$

Then, the conversion for any vector $\vec{y}$ becomes

$$\vec{y}^{\,\text{ECEF}} = \begin{bmatrix} \cos\gamma & \sin\gamma & 0 \\ -\sin\gamma & \cos\gamma & 0 \\ 0 & 0 & 1 \end{bmatrix} \vec{y}^{\,\text{ECI}}$$

Differences in orbits are much more palpable when presented in the Radial, Transversal and Normal (RTN) reference frame. It is defined by the instantaneous state $\vec{r}$, $\dot{\vec{r}}$ of a spacecraft in orbit, as the radial direction $\hat{e}_R$ is given by the position, and the normal direction $\hat{e}_N$ is perpendicular to the orbit plane. The transversal direction $\hat{e}_T$ completes the right-hand system (position and velocity in ECI):

$$\begin{aligned} \hat{e}_R &= \hat{r} = \frac{\vec{r}}{r} \\ \hat{e}_T &= \frac{\hat{e}_N \times \hat{e}_R}{\|\hat{e}_N \times \hat{e}_R\|} \\ \hat{e}_N &= \frac{\vec{r} \times \dot{\vec{r}}}{\|\vec{r} \times \dot{\vec{r}}\|} \end{aligned}$$

Bibliography

[1] National Research Council. *Satellite Gravity and the Geosphere: Contributions to the Study of the Solid Earth and Its Fluid Envelopes*. The National Academies Press, Washington, DC, 1997.

[2] O. B. Andersen, A. Abulaitijiang, L. Stenseng, P. Knudsen, M. Idzanovic, and O. Vegard. The great value of Cryosat-2 SAR and SAR-in for coastal sea level monitoring, March 2017. DTU Space.

[3] National Aeronautics and Space Administration. GRACE launch, March 2002. Press Kit.

[4] Center for Space Research. GRACE spacecraft configuration. `http://www2.csr.utexas.edu/grace/spacecraft/config.html`, February 2004. Last accessed on August 3, 2018.

[5] B. Tapley, J. Ries, S. Bettadpur, D. Chambers, M. Cheng, F. Condi, and S. Poole. The GGM03 mean earth gravity model from GRACE. *Eos Trans. AGU*, 88(52), 2007. Fall Meet. Suppl., Abstract G42A-03.

[6] Tapley B. D., Bettadpur S., Watkins M., and Reigber C. The gravity recovery and climate experiment: Mission overview and early results. *Geophysical Research Letters*, 31(9), 2004.

[7] J. Ries, S. Bettadpur, R. Eanes, Z. Kang, U. Ko, C. McCullough, P. Nagel, N. Pie, S. Poole, T. Richter, H. Save, and B. Tapley. The development and evaluation of the global gravity model GGM05. Technical report, Center for

Space Research, The University of Texas at Austin, May 2016. CSR Report CSR-16-02.

[8] H. Save, S. Bettadpur, and B. D. Tapley. High-resolution CSR GRACE RL05 mascons. *Journal of Geophysical Research: Solid Earth*, 121(10), 2016.

[9] H. V. Save. *Using Regularization for Error Reduction in GRACE Gravity Estimation*. PhD thesis, The University of Texas at Austin, 2009. CSR Report CSR-09-01.

[10] C. M. McCullough. Numerical integration accuracy and modeling for future geodetic missions. Master's thesis, The University of Texas at Austin, 2013.

[11] W. Cheney and D. Kincaid. *Numerical Mathematics and Computing*. Thomson Brooks/Cole, sixth edition, 2008.

[12] B. C. Gunter. *Computational Methods and Processing Strategies for Estimating Earth's Gravity Field*. PhD thesis, The University of Texas at Austin, 2004. CSR Report CSR-04-02.

[13] M. B. Hinga. *Using parallel computation to apply the singular value decomposition (SVD) in solving for large Earth gravity fields based on satellite data*. PhD thesis, The University of Texas at Austin, 2004. CSR Report CSR-04-01.

[14] H. J. Rim. *TOPEX Orbit Determination Using GPS Tracking System*. PhD thesis, The University of Texas at Austin, 1992. CSR Report CSR-92-03.

[15] J. R. Kim. *A Simulation Study of a Low-Low Satellite-to-Satellite Tracking Mission*. PhD thesis, The University of Texas at Austin, 2000. CSR Report CSR-00-02.

[16] J. B. Thomas. An analysis of gravity-field estimation based on intersatellite dual-1-way biased ranging. Technical report, Jet Propulsion Laboratory, Pasadena, California, May 1999. JPL Publication 98-15.

[17] S.-C. Wu, G. Kruizinga, and W. Bertiger. *Algorithm Theoretical Basis Document for GRACE Level-1B Data Processing V1.2.* Jet Propulsion Laboratory, Pasadena, California, May 2006. JPL D-27672.

[18] S. V. Bettadpur. *UTCSR Level-2 Processing Standards Document.* Center for Space Research, The University of Texas at Austin, April 2018. Rev 5.0 (For Level-2 Product Release 0006).

[19] D. E. Cartwright. *Tides: A Scientific History.* Cambridge University Press, 1999.

[20] A. T. Doodson. The harmonic development of the tide-generating potential. *Proceedings of the Royal Society of London A: Mathematical, Physical and Engineering Sciences*, 100(704):305–329, 1921.

[21] D. E. Cartwright and R. J. Tayler. New computations of the tide-generating potential. *Geophysical Journal of the Royal Astronomical Society*, 23(1):45–73, 1971.

[22] National Aeronautics and Space Administration. Greenland's eastern coast. `https://upload.wikimedia.org/wikipedia/commons/c/c2/Greenland.A2003233.1340.250m.jpg`, November 2005. Last accessed on August 3, 2018.

[23] J. H. Ferziger. *Numerical methods for engineering application.* Wiley, 1981.

[24] International Astronomical Union. *Resolution A4: Recommendations from the Working Group on Reference Systems*, 1991.

[25] Astronomical Applications Department US Naval Observatory. Approximate sidereal time. `http://aa.usno.navy.mil/faq/docs/GAST.php`, 2011. Last accessed on August 3, 2018.